Phonon analogues to the topological Su-Schrieffer-Heeger (SSH) model

Abdulla Alseiari

Department of Physics

McGill University, Montreal

December, 2022

A thesis submitted to McGill University in partial fulfillment of the requirements of the degree of

Master of Science

Abstract

This thesis examines the topological phonon phases of realistic isotope superlattices (ISL). It is shown that, in one dimension, the ISL can be mapped onto the Su–Schrieffer–Heeger (SSH) model and exhibits a similar topological phase transition after some transformation. The transformation we considered is the differences between neighboring displacements instead of the displacement alone. Then, a worked-out phononic crystal (PC) design is presented using experimental material data, which exhibits a topological phase transition. The PC is a beam of alternating radii lengths made of stainless steel. Finally, using Langevin baths, the heat transport of the ISL is evaluated for the different phases. The model demonstrated a potential heat rectification device.

Abrégé

Cette thèse examine les phases de phonons topologiques de super-réseaux isotopiques (SRI) réalistes. Il est montré que, dans une dimension, le SRI peut être mis en correspondance avec le modèle de Su-Schrieffer-Heeger (SSH), qui présente une transition de phase topologique similaire après avoir effectué une certaine transformation. La transformation que nous avons considérée considère la différence entre les déplacements voisins au lieu du déplacement seul. Nous présentons ensuite un modèle de cristal phononique (CP) élaboré à l'aide de données matérielles expérimentales, qui présente une transition de phase topologique. Ce CP est cylindre de de rayons alternés en acier inoxydable. Enfin, à l'aide de bains thermiques de Langevin, le transport de chaleur du SRI est évalué pour les différentes phases. Le modèle a démontré un dispositif potentiel de rectification de la chaleur.

Acknowledgements

I want to express my gratitude to my supervisor, Professor Michael Hilke, who guided me throughout this project. I also want to thank my twin brother, Abdulrahman, for assisting me with Matlab and Latex and supporting me during the past few years. My biggest thanks goes out to my kids; sorry for being absent most of the day working on my thesis! For my wife, thanks for all your support in taking care of some of my responsibilities, which allowed me to focus more on my studies. I also want to thank my family and friends who supported me and offered deep insights into the study.

Table of Contents

List of Figures

List of Tables

Chapter 1

Overview

1.1 Topology

In 1741, Leonhard Euler proposed a solution to the Königsberg bridge problem, a mathematical puzzle involving seven bridges on two landmasses and an island in a town called Königsberg [1]. The question was whether a person could walk through the town while only crossing each bridge once. His solution led to the development of a field of mathematics known as topology.

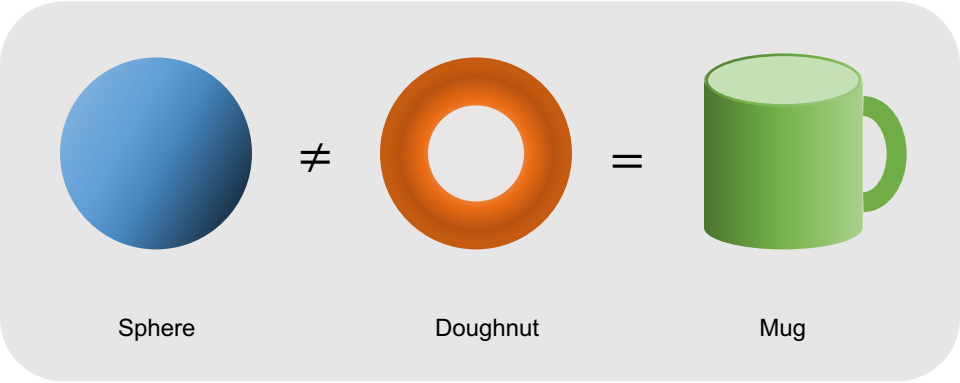

Figure 1.1: Example of three topological objects where the mug and doughnut are topologically equivalent while the sphere is not.

Topology is a field in mathematics that studies the attributes of geometrical object deformations. Topology classifies geometrical objects into two categories: topologically

equivalent and topologically distinct. Geometrical objects that can be deformed without creating or closing a hole, tearing or gluing, nor passing through themselves are topologically equivalent. Homeomorphism and homotopies deformations in topology are the only allowed deformations that preserve an object's topology [2]. Homeomorphism is the one-to-one mapping of a continuous function between topological spaces with an inverse function. An example is when an object undergoes continuous bending and stretching into a new shape. Under smooth deformations, two geometrical objects' properties are invariant if the properties do not change, while we deform them into each other without losing the properties. A well-known example is a sphere, a doughnut, and a coffee mug, as shown in Figure 1.1. A sphere is deemed topologically distinct from a doughnut and a coffee mug, while the doughnut and coffee mug are considered topologically equivalent. The topological invariant, in this case, is the genus number g, which represents the number of holes the object has. This example is concerned with objects' surfaces, and to define the topological invariant as in reference [3], we use the Gauss-Bonnet theorem, as follows:

$$\chi = \frac{1}{2\pi} \int_S K dA \tag{1.1}$$

where χ is the Euler characteristic for a sphere of radius R is 2 and $K = 1/R^2$ is the gaussian curvature, here related to the genus number g by $\chi = 2 - 2g$.

In summary, any two geometrical objects that can be deformed into each other are topologically equivalent if their topological properties are invariant. Then, the most crucial question is what topological invariants is the one that characterizes the system. A critical example of a topological invariant in the field of topological condensed matter is the winding number, which we will discuss later in chapter two.

1.2 Topological insulators

Topological phases are a new domain of physics that has gained attention since the quantum Hall effect was first discovered in 1980 by Von Klitzing [4]. The quantum Hall effect is considered to be the first known topological phase. Topological phases can exist in 1D [5], 2D [6], or 3D [7] geometrical objects. Not only are quantum systems topological phases, but classical systems also can exhibit topological phases [8]. The materials that demonstrate the quantum Hall effect are considered a subset of materials classified as topological insulators. In general, insulators are the materials with an energy gap splitting the excited state electrons from the ground state. This separation of states permits topological classification founded on adiabatic continuity. Two insulating materials are equivalent if their Hamiltonian can be gradually transformed from one to the other so that the system constantly stays in the ground state. The energy gap determines how slowly the adiabatic process should be, if possible. A topological insulator is a material conducting at the outside boundary and insulating at the inside bulk. To understand topological insulators, we can start with the Su–Schrieffer–Heeger (SSH) model, which is a 1D model [9]. This 1D model is essential because, despite its simplicity, it will make understanding the fundamental concepts in topological insulators easier. In chapter two, we will start with defining metals and their properties while touching base on conducting and insulating band gaps. Then, we will introduce the SSH model and define the meaning of topology in a 1D material. By the end of the second chapter, we will summarize the experimental results and describe some potential applications of topological insulators.

1.3 Topological phononics

In recent years, physicists have been working on a phononic version of the SSH model. Mass-spring models as a representation of the SSH model have been proposed to understand the topological phases in phonons and photons. The most common method is replacing the hopping amplitudes (electron site) of the SSH model with the spring (mass)

in the Mass-spring model [10]. Other proposed modifications can be obtained by adding fixed/heavy masses at the edges to preserve the chiral symmetry of the model in 1D [11]. In 2D, one way to preserve chiral symmetry was by introducing a dent beneath the Mass-spring model floor [12]. The emerging phononic topology field will allow scientists to exploit phonons and develop new material [10]. Some candidate materials are currently being investigated to show the phononic topology. Tungsten diselenide and sodium chloride [13], graphene [14], and silicon [15] are a few examples of explored materials that show the topological behavior of phonons. The potential of phononic topology applications ranges from topological quantum computation [16], to phononic devices [17], and topological phononic materials [18]. In chapter three, we explain phonons from a classical point of view and discuss some important features of a diatomic chain. Then, chapter four will discuss our work to look at the diatomic chain topologically and discuss its similarities with the SSH model.

1.4 Topological heat transport

Heat transport is an essential and well-established topic in many fields. The importance of heat transport can be seen in every house and new technology, from smartphones to electric cars, in nanoscale systems, and in mega constructions. However, topological heat transfer is a new area that started to earn attention in the last couple of years. The recent interest in topological heat transport is because of the latest advances in developing topological materials. Heat transport started with Fourier's law of heat conduction in 1822, which is a phenomenological law. Heat transport is a well-studied topic; however, at low dimensions, there is no single model that can work for all cases. Our focus will be on 1D models, precisely the heat baths method. The most common heat bath method is the Langevin bath, which we will discuss in more detail in chapter five. In 2012, Kannan, Dhar, and Lebowitz [19] analyzed the heat transport in a chain of alternating masses, showing an even–odd number of masses dependency. Then, in 2017, a group of physi-

cists [20] used the Langevin baths to find an analytical solution for the thermal conductance of a system with alternating masses by using nearest neighboring coupling. In 2018, another group studied the topological thermal effects in classical dimerized micro- and nanomechanical lattices [21]. Chapter five will examine the results of applying the Langevin baths method to our 1D phononics model.

Chapter 2

SSH model

In this chapter, we examine the SSH model in more detail. Physicists developed many models to understand topological insulators. The SSH model is a 1D model invented by Wu Su, John Schrieffer, and Alan Heeger in 1979 to understand a polyacetylene polymer [9], which was an attempt to explain the increased electrical conductivity of doped polyacetylene polymer. The tight binding model describes spinless electrons hopping in a chain of alternating two bond types. Even though it is a 1D model, the basic concepts we will learn will apply to 2D and 3D models. This chapter is strongly inspired by references [22, 23].

2.1 Metals

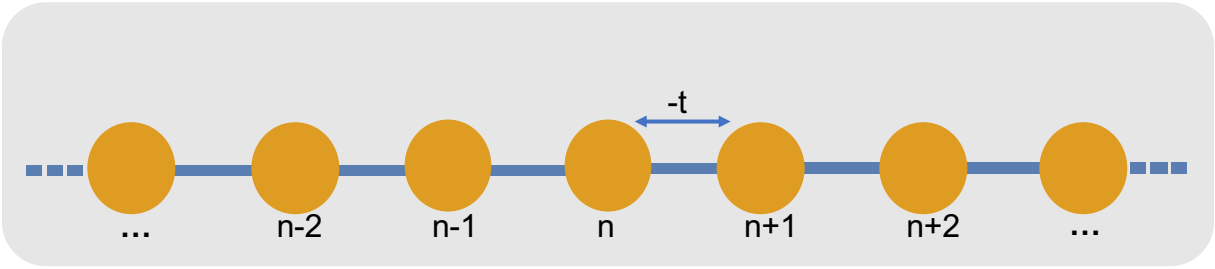

Figure 2.1: 1D tight binding Hamiltonian representation.

This section will explain the basic concepts and tools physicists use to distinguish a conductor from an insulator. We start with a 1D tight-binding model of the crystal lattice of atoms, as seen in Figure 2.1. As we move these atoms toward each other, their eigenstates overlap, so their wave functions form bonding and anti–bonding states. This overlapping allows the electrons to delocalize and tunnel inside this chain of atoms. We represent the tunneling potential by $-t$, as shown in Figure 2.1. The Hamiltonian of this model is as follows:

$$H = -\sum_{i,j}^{N} t_{i,j} \left|i\right\rangle \left\langle j\right| \tag{2.1}$$

where i and j are the lattice sites and t_{ij} is the overlap integral between these two sites. Because i and j are independent, we can impose $t_{ij} = t_{ji}$, and it is clear that t_{ii} corresponds to the onsite potential. Thus, the Hamiltonian becomes Hermitian (assuming t_{ij} is real). Now, we define the translation operator as $T = \sum_i \left|i+1\right\rangle \left\langle i\right|$. Assuming that $t_{i,i+n} \equiv t_n$, and onsite potential $t_{ii} = 0$, the Hamiltonian becomes the following:

$$H = -\sum_{n} t_n T^n + h.c \tag{2.2}$$

Because H and T commute ($[H, T] = 0$), using the following plane wave basis states, which is an eigenbasis of the translation operator, we can diagonalize the Hamiltonian in equation (2.1):

$$\left|k\right\rangle = \frac{1}{\sqrt{N}} \sum_{j} e^{ikj} \left|j\right\rangle \tag{2.3}$$

Acting on $\left|k\right\rangle$ by the translation operator, we get $T^m \left|k\right\rangle = e^{ikma} \left|k\right\rangle$, where a is the lattice constant and, in our case, the lattice spacing between the two atoms. Thus, the Hamiltonian has eigenvalues $\epsilon(k)$ where $H \left|k\right\rangle = \epsilon(k) \left|k\right\rangle$. The eigenvalues are as follows:

$$\epsilon(k) = -\sum_{n} t_n e^{-ikna} + c.c \tag{2.4}$$

By only allowing hopping to the nearest neighbor and setting $t_1 = t$ and all other $t_n = 0$, we get the following:

$$\epsilon(k) = -2t \cos ka \tag{2.5}$$

Plotting E $vs.$ k is the dispersion relation (as seen in Figure 2.2). We call the range of k from $-\pi/a$ to π/a the Brillouin zone. The Brillouin zone's importance comes from illustrating the system's behavior, and it is convenient to choose the Fermi energy equal to zero (because energies are always measured with respect to how far they are from the Fermi energy in condensed matter physics). Because of the Pauli principle, the maximum available occupancy is two electrons for the same momentum state. The edges of k ($k = \pm\pi/a$) are called the Brillouin zone edges, and as we can see, there are no gaps and electrons can hop between atoms. Therefore, this model represents a metal.

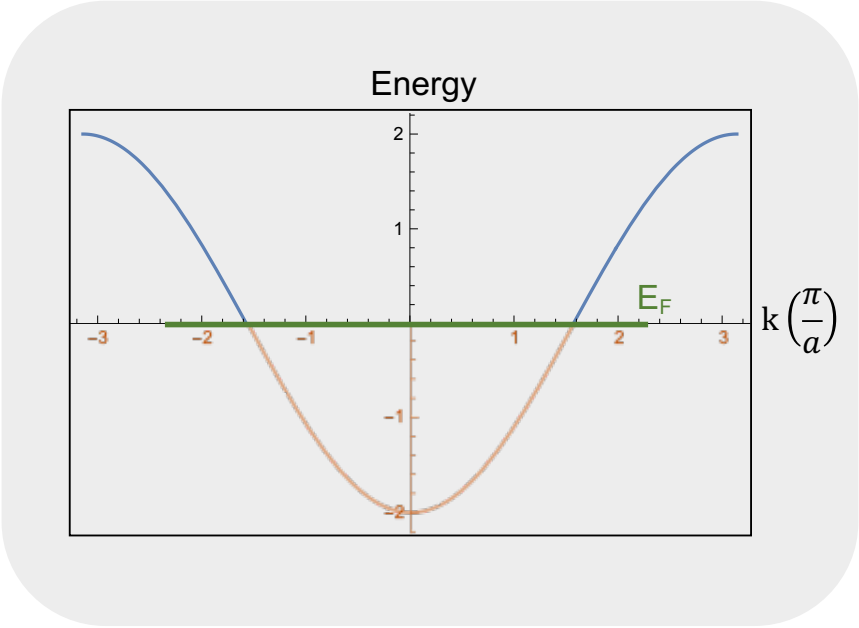

Figure 2.2: Energy dispersion relation of a 1D tight binding Hamiltonian. The orange curve represent the filled states.

2.2 Band insulators

Let us take the same model as in the previous section but with slight modifications. In the previous model, we assumed the presence of hopping between periodic atoms (as seen in Figure 2.3). In this section, we will assume free electrons with parabolic dispersions of the form $E = h^2k^2/2m$. Similar to the previous section, placing one electron per lattice site will result in a no-gap Brillouin zone, and the system acts like a metal. Nevertheless, in the 1930s, Rudolf Peierls showed that this system was unstable and prone to distortion regardless of choice of dispersion.

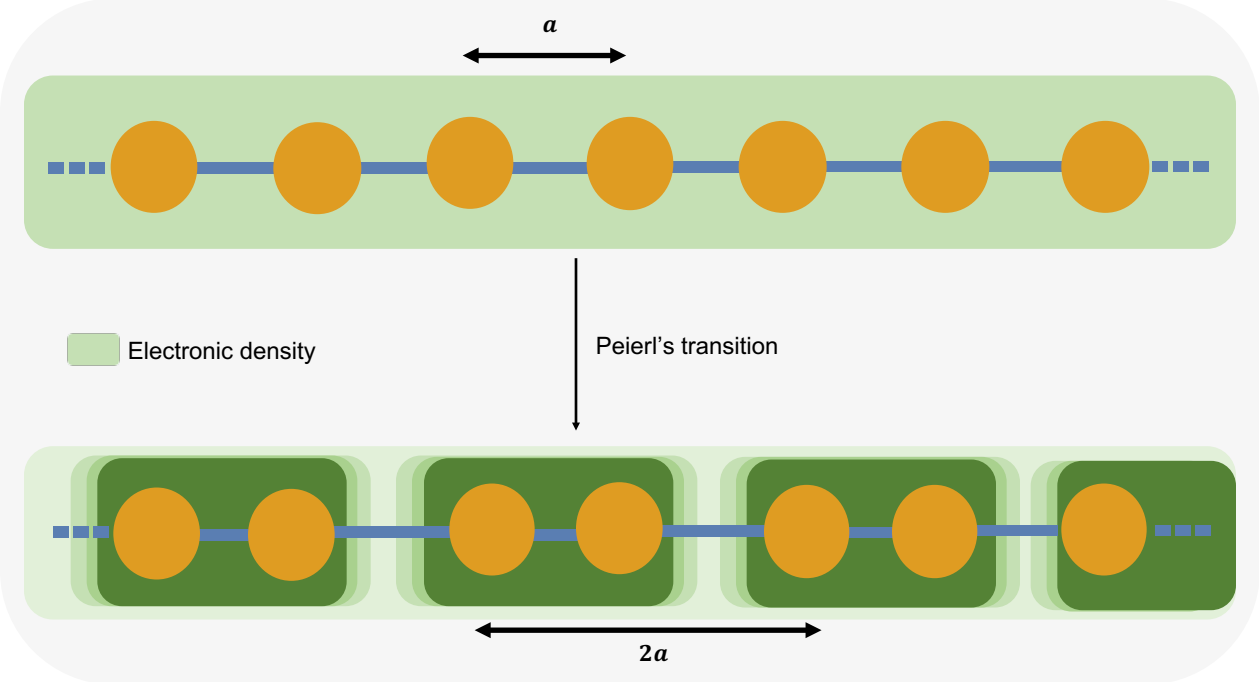

Figure 2.3: 1D lattice that undergoes a Peierl's transition. Lattice constant a becomes $2a$ after distortion. The darker regions represent electronic density.

Now, let us consider the model in the previous section where the atoms have spacings of a; here, we have a uniform electric density. By distorting the system by moving every two atoms toward each other, as in Figure 2.3, the lattice has two atoms per unit cell. The system has unit cells with interunit cell spacing of $2a$ and periodically modulated electric density, which is called the charge density wave. The distorted system has a total energy

greater than the undistorted system. We can estimate the energy of the system, as in [24], using the elastic approximation, as follows:

$$\Delta E_{lattice} = \frac{1}{4} K \delta^2 \tag{2.6}$$

where K is the elasticity constant determined by the material and δ is the distortion, which is quadratic. In the low distortion limit, the electric energy per unit length is approximately:

$$\Delta E_{electric} \approx \frac{A^2 \delta^2}{\pi} \ln |\delta| \tag{2.7}$$

where A is the proportionality constant, loosely saying it represents some kind of coupling between the electrons and phonons. The total energy per unit length is $\Delta E_{lattice} + \Delta E_{electric}$ and can be optimized as follows:

$$\frac{d}{d\delta}[\Delta E_{total}] = \frac{1}{2} K \delta + \frac{2A^2}{\pi} \delta \ln |\delta| + \frac{A^2}{\pi} \delta = 0 \tag{2.8}$$

By calculating the second derivatives, we can check that the maxima are at $\delta = 0$ and the minima correspond to:

$$\delta_{min} = \pm e^{-1/2} e^{-ka/4\pi} \tag{2.9}$$

By substituting δ_{min} into E_{total}, we get a negative change in energy. Thus, the system gains energy by distorting itself by δ_{min}; this is known as Peierl's instability. Plotting the Brillouin zone for this system as in Figure 2.4, we see that the periodicity is doubled, and the Brillouin zone edges are from $k = +\frac{\pi}{2a}$ to $k = -\frac{\pi}{2a}$. This doubling in the periodicity causes the Brillouin zone to have a bandgap, as seen in Figure 2.4. This bandgap separates the filled states from the empty states at the new Brillouin zone edges, making the system a band insulator.

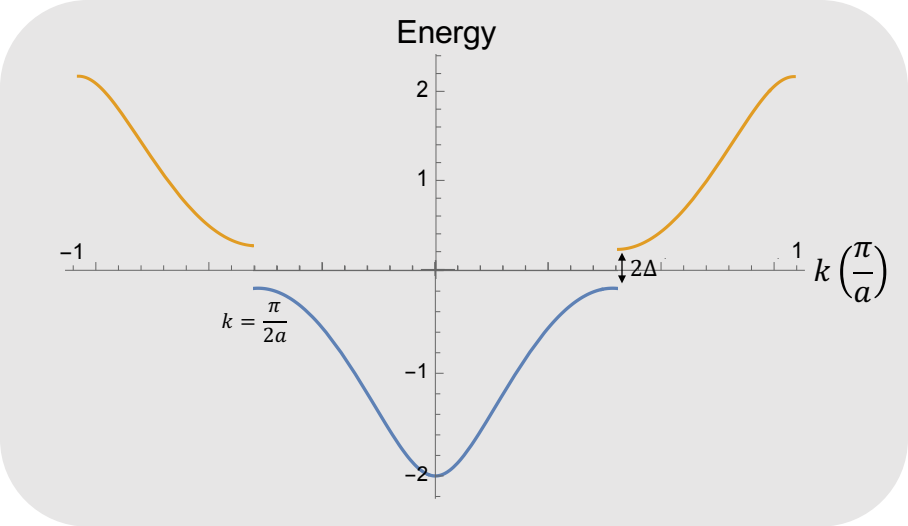

Figure 2.4: The dispersion after lattice distortion, where the new Brillouin zone boundary is $k = \pm\frac{\pi}{2a}$

2.3 SSH model

In 1979, Su, Schrieffer, and Heeger (SSH) introduced a model to describe a 1D carbon molecule called polyacetylene. Polyacetylene is a chain of repeating units (C2H2) with alternating bonds between the carbon atoms (see Figure 2.5). We denote the unit cell of two carbon atoms by atom A and atom B, where the bonds are $t(1-\delta)$ and $t(1+\delta)$. Thus the second quantized Hamiltonian is as follows:

$$H = t\sum_{i=1}^{L}[(1-\delta)c_{A,i}^{\dagger}c_{B,i} + (1+\delta)c_{B,i}^{\dagger}c_{A,i+1} + h.c.] \tag{2.10}$$

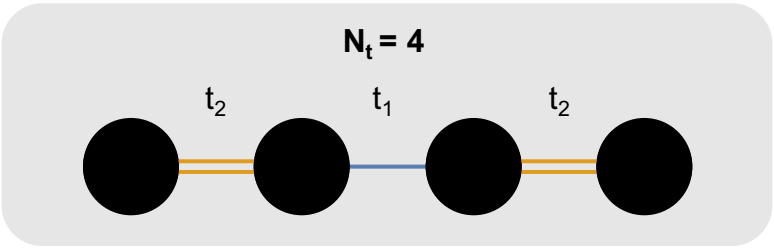

Figure 2.5: 1D chain of the SSH model.

where i is indexing the unit cell, and $c^\dagger$ and c are the creation and annihilation operators, respectively. These operators satisfy the anticommutation relations and have the following properties:

$$\begin{aligned} \{c_i, c_j^\dagger\} = \delta_{i,j} \qquad & \{c_i, c_j\} = 0 \\ c^\dagger |0\rangle = |1\rangle, \qquad & c|0\rangle = 0 \\ c^\dagger |1\rangle = 0, \qquad & c|1\rangle = |0\rangle \end{aligned} \tag{2.11}$$

To rewrite the Hamiltonian in the momentum space, we use the translation symmetry of the chain to solve for the dispersion relations such that:

$$c_{\alpha,i} = \frac{1}{\sqrt{L}} \sum_k e^{i\vec{k}\cdot\vec{r_i}} c_{k,\alpha} \tag{2.12}$$

$$H = \sum_{\alpha \in A,B} c_{\alpha,k}^\dagger h_{\alpha\beta}(k) c_{\beta,k} \tag{2.13}$$

$$H(p)_k^{\alpha\beta} = \begin{bmatrix} 0 & t(1-\delta) + t(1+\delta)e^{ika} \\ t(1-\delta) + t(1+\delta)e^{-ika} & 0 \end{bmatrix} \tag{2.14}$$

For simplicity, we set the lattice spacing $a = 1$ and $t = 1$. We can write the Hamiltonian using the Pauli matrices as follows:

$$H_k^{\alpha\beta} = [(1-\delta) + (1+\delta)\cos k]\sigma_x + [(1+\delta)\sin k]\sigma_y + 0 \cdot \sigma_z + 0 \cdot \mathbb{I} \equiv \vec{d_k} \cdot \vec{\sigma} + \epsilon_k \sigma_0 \tag{2.15}$$

where $\epsilon_k = 0$ and $\mathbb{1} = \sigma_0$, the vector $\vec{d_k}$ is:

$$\vec{d_k} = ((1-\delta) + (1+\delta)\cos k, (1+\delta)\sin k, 0) \tag{2.16}$$

This Hamiltonian can be diagonalized in terms of $\vec{d_k}$ and ϵ_k, and the outcome is two bands:

$$E_k^{\pm} = \pm\left|\vec{d_k}\right| + \epsilon_k = \pm\sqrt{d_x^2 + d_y^2 + d_z^2} + \epsilon_k \tag{2.17}$$

which in this case is:

$$\begin{aligned} E_k^{\pm} &= \pm\sqrt{((1-\delta) + (1+\delta)\cos k)^2 + ((1+\delta)\sin k)^2} \\ &= \pm\sqrt{(1-\delta)^2 + 2(1-\delta^2)\cos k + (1+\delta)^2} \\ &= \pm\sqrt{2 + 2\delta^2 + (2-2\delta^2)\cos k} \end{aligned} \tag{2.18}$$

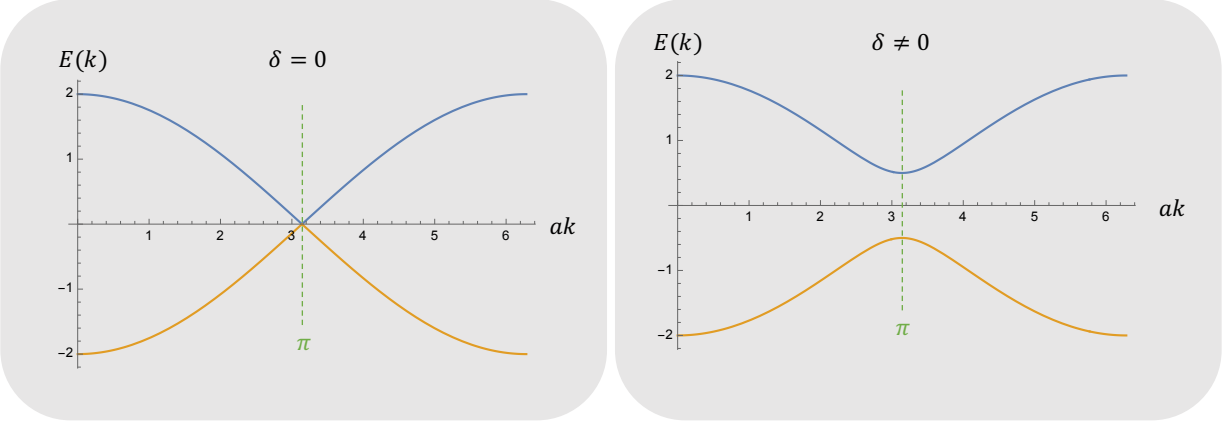

Figure 2.6: The dispersion relation of SSH model, where $\delta = 0$ is gapless and $\delta \neq 0$ has a gap.

We can see the resulting bands in Figure 2.6. For $\delta = 0$, the dispersion relation is gapless. When δ is finite, the model is dimerized and the dispersion relation is gapped.

Let us focus on the gapped system. The condition that $\left|\vec{d}_k\right| \neq 0$, which is the condition of no energy levels crossing, means that all $\vec{d}_k$ does not hit the origin point $\vec{d} = (0, 0, 0)$. Plotting the vector in the (d_x, d_y) plane, changing k results in two types of closed paths where one encircles the origin and the other does not, depending on the delta value, as shown in Figure 2.7.

This result means that we have two distinct types of insulators that cannot be connected unless we cross a gapless point. This property is only possible because $dz = 0$,

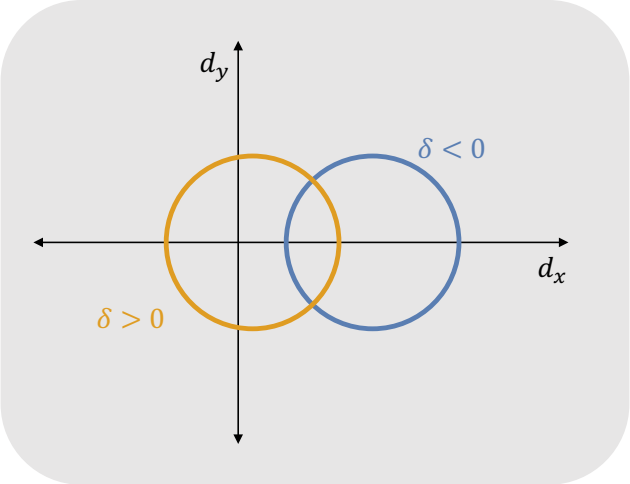

Figure 2.7: Parameter space where the two closed lines represent two different paths by varying k while δ is fixed at either $>$ or $<$ than 0, while the gapless point located at the origin.

which is imposed by chiral symmetry ($\hat{S}$) and inversion and time–reversal symmetry ($\hat{T}\hat{I}$). We will discuss chiral symmetry in the next section.

The $\delta > 0$ and $\delta < 0$ represent two different topological phases. The way to distinguish between these two topological phases is by introducing a topological property called the winding number. A winding number is an integer that represents the number of times the path encircles the origin, as shown in Figure 2.7. For the SSH model, the winding number is either 1 or 0. The winding number is a topological invariant, also called an adiabatic invariant, which describes an insulating Hamiltonian that does not change under adiabatic deformations.

2.4 Chiral Symmetry

Before we discuss winding numbers and polarization, we need to understand chiral symmetry. The concept of symmetries is essential to classify topological insulators; however, we can see topological phases without looking at symmetries. Symmetry is a mathematical tool that makes the math involved in the concepts of condensed matter models simple.

Chiral symmetry is a unitary and anticommutative matrix with a hamiltonian h, which is equal to the combination of two nonunitary symmetries. Chiral symmetry is defined as follows:

$$\hat{S} = \hat{C} \cdot \hat{T}$$

where $\hat{C}$ is the particle-hole symmetry and $\hat{T}$ is the time-reversal symmetry. The time-reversal symmetry is defined as an operator that takes the time t to time $-t$. At the same time, particle-hole symmetry is defined as an operator that turns particles into holes (i.e., particle annihilation). The chiral symmetry matrix always squares to 1 ($\hat{S}^2 = 1$), so chiral symmetry is either present or absent, depending on the particle-hole symmetry and time-reversal symmetry combinations. We end up with 10 possibilities, as shown in Table 2.1.

$\hat{S}$	$\hat{C}$	$\hat{T}$
1	+1	+1
1	-1	-1
1	-1	+1
1	+1	-1
0	0	+1
0	0	-1
0	+1	0
0	-1	0
1	0	0
0	0	0

Table 2.1: This table shows all possible topological properties of different systems' symmetries. The three integers $(0, 1, -1)$ means there is either no symmetry, there is symmetry and it squares to $+1$, there is symmetry and it squares to -1, respectively.

This table is called the 10-fold classification, which classifies different topological properties for different systems depending on the system's symmetries and dimensionality.

2.5 SSH winding number and polarization

By the end of the section 2.3, we mentioned the winding number and how it classifies two distinct topological phases. Before we discuss the SSH winding number, we need to define a winding number. For any bounded region R, the local winding number is defined as the number that equals how many times the curves are bounding R counterclockwise minus the times the curves bound R clockwise. Figure 2.8 shows a few examples of the winding number.

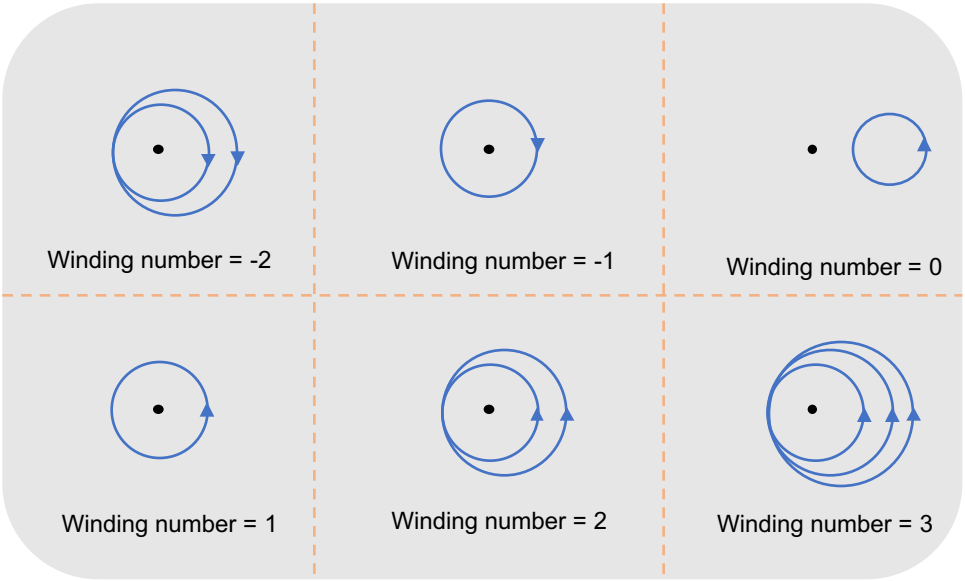

Figure 2.8: Examples of regions with different winding numbers.

For the SSH model, we need to look at how many times d_k winds the origin. We can represent any single particle Hamiltonian with chiral symmetry as follows:

$$h(k) = \begin{bmatrix} 0 & q_k \\ q_k^\dagger & 0 \end{bmatrix} \tag{2.19}$$

where $q_k = d_x(k) - id_y(k)$. The winding number for this Hamiltonian is defined in [22] as follows:

$$v = \frac{i}{2\pi} \int_k \mathrm{Tr}\left[q_k \partial_k q_k^\dagger\right] \tag{2.20}$$

Now, we will discuss the polarization, and by the end of this section, we relate it to the winding number. From quantum mechanics, we know that the total polarization P is the sum of all occupied bands' polarization. Here, the polarization of each occupied band, as defined in the reference [23], is as follows:

$$P_n = -\frac{e}{2\pi}\int_0^{2\pi} dk \, \langle u_k^n | \, i\partial_k \, | u_k^n \rangle \equiv \frac{e}{2\pi}\Phi_n \tag{2.21}$$

$$P_{total} = \sum_{n \in occupied} P_n \tag{2.22}$$

where n is defined as the occupied band index that has a corresponding eigenvector $|u_k^n\rangle$. Performing the above differentiation and integration, we get the following SSH total polarization:

$$P_{total} = \frac{e}{2} \mod e \tag{2.23}$$

Previously, we defined two bands for the SSH model. One is $\delta > 0$, and the other is $\delta < 0$. $\delta = \pm 1$ are extreme cases of dimerization which could give more intuition. Let $\delta = 1$; then, the eigenvector is:

$$\left|u_k^{\pm}\right\rangle = \frac{1}{\sqrt{2}} \begin{bmatrix} \mp e^{ik} \\ 1 \end{bmatrix} \tag{2.24}$$

where the $E_k = \mp 1$. Because the SSH model has spatially separated charges, these charges produce polarization.

On the other side, for $\delta < 0$, let $\delta = -1$. The eigenvector is:

$$\left|u_k^{\pm}\right\rangle = \frac{1}{\sqrt{2}} \begin{bmatrix} \pm 1 \\ 1 \end{bmatrix} \tag{2.25}$$

where $E_k = \pm 1$. Following the same steps as the one for $\delta = 1$, we get the total polarization for $\delta = -1$ as follows:

$$P_{total} = 0 \mod e \tag{2.26}$$

The following equation relates the polarization and winding numbers:

$$P = e\frac{v}{2} \mod e \tag{2.27}$$

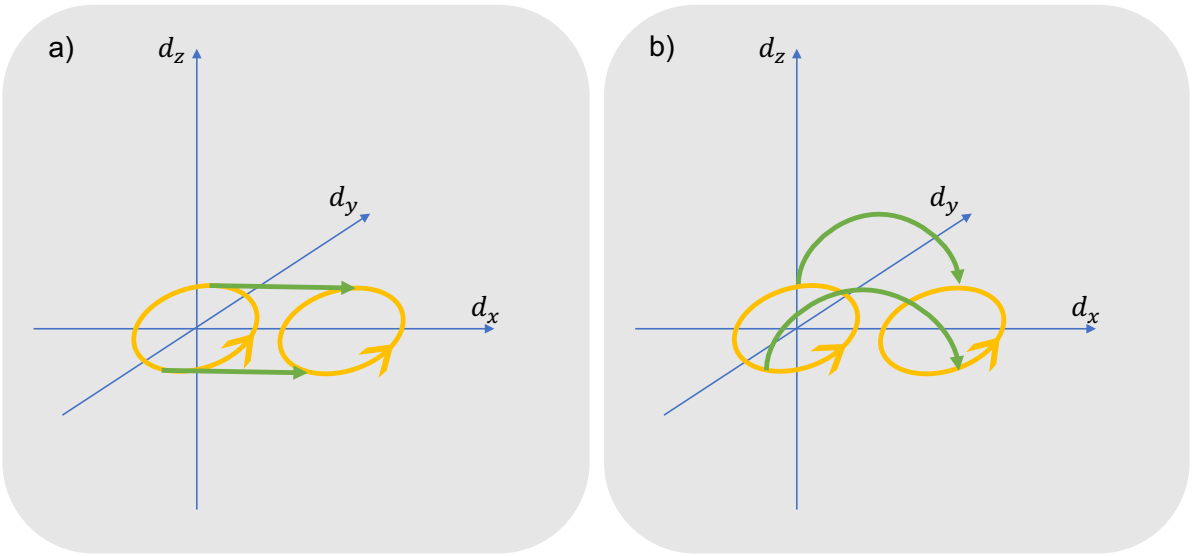

Figure 2.9: Two ways to close the gap, where $a)$ shows closing the gap without breaking the chiral symmetry and $b)$ shows breaking the chiral symmetry case.

The winding number for the SSH is either 0 or 1, and to change it from one to the other, we must either break the chiral symmetry or close the bulk gap, as shown in Figure 2.9. We need to examine the edge states to understand the physical differences between various winding numbers.

2.6 Edge states

The SSH Hamiltonian has a bulk and edge, and this distinction between the two parts of the material helps us understand the energy eigenstate behaviors. In the thermodynamic limit where $\delta = 1$ and $\delta = -1$, the edge state's emergence and absence are apparent, as

shown in Figure 2.10. We call these two simple cases the two fully dimerized cases, where the SSH chain dissociates into a detached sequence of dimers.

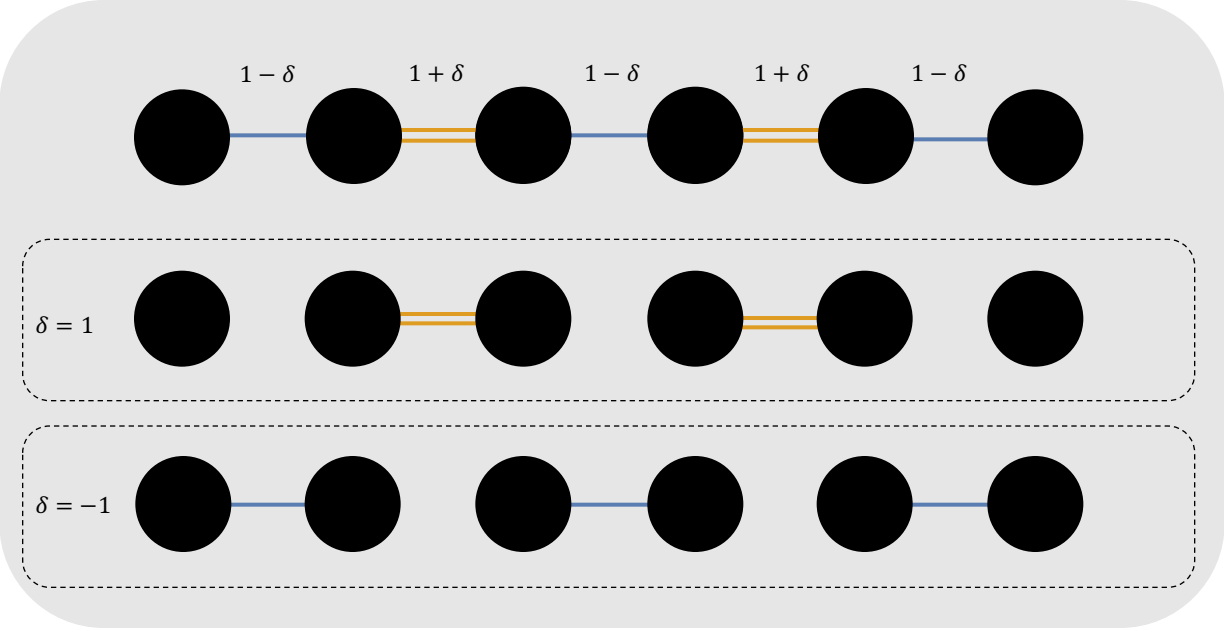

Figure 2.10: 1D chain of the SSH model where two limits illustrate the edge states.

Looking at the bulk in the fully dimerized limits, we have two cases: the trivial case and a topological case. In the trivial case where $\delta = -1$, the momentum-space Hamiltonian of the bulk is $H(k) = \sigma_x$, which is independent of the wavenumber k. While in the topological case, where $\delta = 1$, the bulk momentum-space Hamiltonian is $H(k) = \sigma_x \cos k + \sigma_y \sin k$. The energy eigenvalues of these two fully dimerized limits are $E(k) = \pm 1$, which is independent of the wave number k. The particles in these limits are not moving along the chains because the chain consists of disconnected dimers.

In the topological case, we can see the most straightforward example of edge states because at the edges of the SSH chain, each edge hosts a single eigenstate. Because of chiral symmetry, the edge states have zero energies because the SSH model forbids onsite potentials. Hence, this creates states at the edge that require zero energy.

After establishing the fully dimerized limit, we can move away to a more general case. By varying the delta from 1 to -1, we can examine the finite SSH model's energy spectrum and wave functions, as shown in Figure 2.11 (adapted from [25]). As we can see, the edge

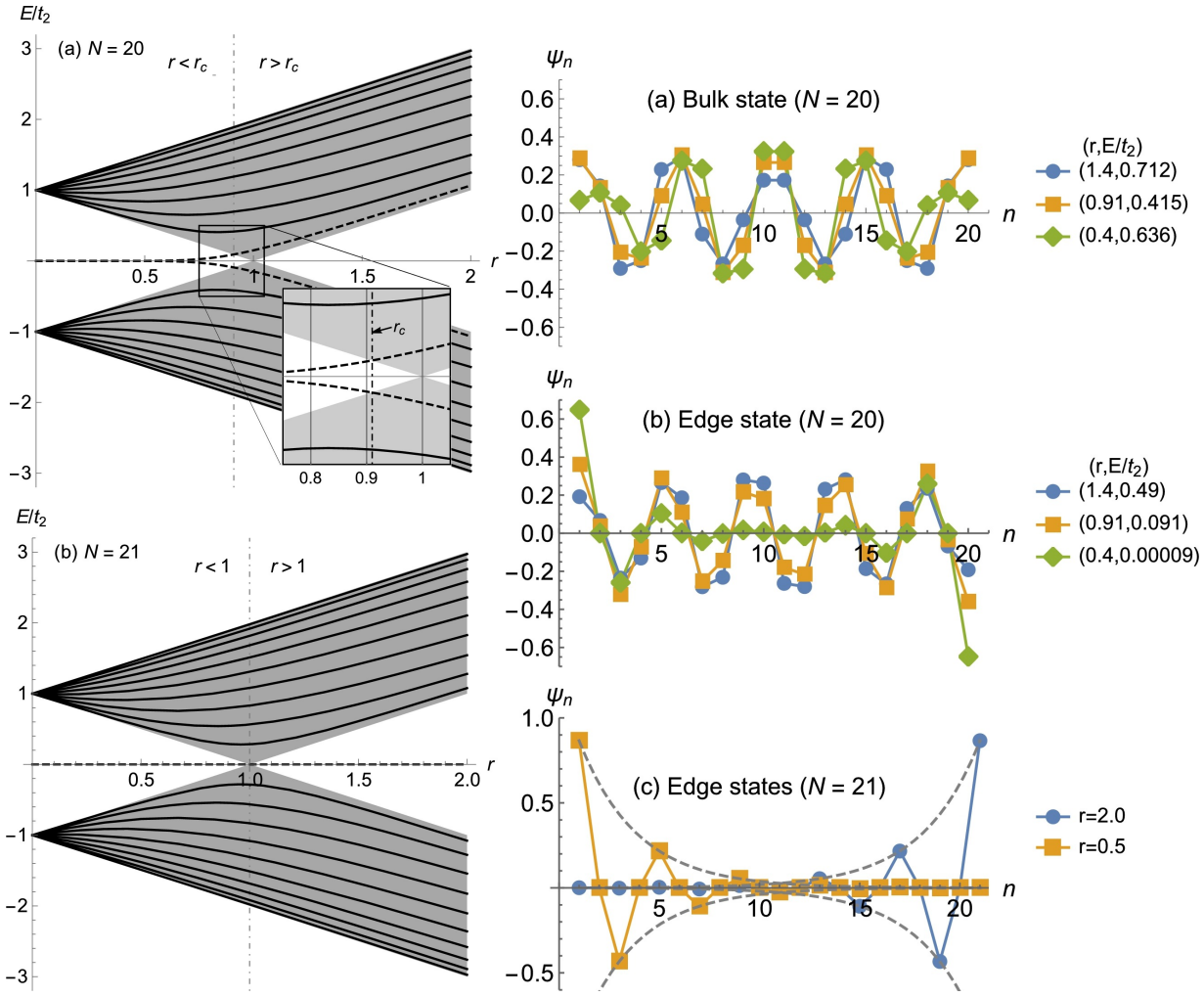

Figure 2.11: The left two plots show the energy spectrum of a finite size ($N = 20$ and $N = 21$) SSH model. The right three plots show the wave functions of an SSH model. a) shows the bulk state wave function of a SSH model of size 20. b) and c) show the edge states of an SSH model of sizes 20 and 21, respectively. Here, r is the hopping parameters ratio ($r = t_1/t_2$), and r_c is where the edge states are located in the band edge

states, which have nearly zero energies, have localized wave functions at the edge cells. The next few sections will look into the edge states' effects and how they relate to the winding number and bulk-boundary correspondence.

2.7 Number of Edge states

Assume a gapped Hamiltonian in the thermodynamic limit $N \to \infty$; each unit cell has two nonzero states that are chiral symmetric partners, that is, one is positive and the other is negative. In contrast, the zero energy states are finite and limited to a single sublattice (as shown below) such that there are N_A states for sublattice A and N_B states on sublattice B. The number $N_A - N_B$ is conserved and can be explained by applying an adiabatic deformation, as follows:

1. Let d be a continuous parameter defined as $d : 0 \to 1$. Take into account the energy eigenstates in the thermodynamic limit at the left end of a gapped chiral symmetric one dimensional Hamiltonian in an energy window from $-\epsilon < E < \epsilon$ with ϵ in the bulk gap. For all values of d, the energy of the bulk gap exceeds 2ϵ because the Hamiltonian respects chiral symmetry.

2. For $d \geq d'$ (d' is the point where the deformation moves a zero energy state $|\Psi_0\rangle$ to energy $E > 0$), the deformation moves a nonzero energy edge state $|\Psi_0(d = 0\rangle$ to be zero energy $E_0(d) = 0$.

3. $\Gamma\,|\Psi_0(d)\rangle$, which is the chiral symmetric partner of $|\Psi_0(d)\rangle$, moves simultaneously to be zero energy states.

These new zero energy edge states are $P_A\,|\Psi_0(d')\rangle$ on sublattice A and $P_B\,|\Psi_0(d')\rangle$ on sublattice B; therefore, the number $N_A - N_B$ is conserved. During this deformation, the initial zero energy state $|\Psi_0\rangle$ becomes negative in energy at some point $d = d'$. At the same time, another state must be created with positive energy, which is a chiral symmetric partner. In this case, both N_A and N_B decrease by 1, so $N_A - N_B$ does not change. In addition, nonzero energy states can move in or out of the $-\epsilon < E < \epsilon$ energy window during the deformation, but this does not affect $N_A - N_B$. For the wavefunctions of the zero energy states, the gap condition forbids edge states from having any shape other than exponential decay toward the bulk wavefunction, which implies that $N_A - N_B$ must remain

unchanged. These previous discussions demonstrate that $N_A - N_B$ are conserved; thus, they are a topological invariant.

2.8 Bulk-boundary correspondence

After introducing the two topological invariants, the winding number, and the number of edge states $(N_A - N_B)$, we will investigate the bulk-boundary correspondence. The bulk-boundary correspondence is simply the relationship between the two topological invariants. We can predict the edge states' low energy physics using the winding number invariant. We used the bulk Hamiltonian to solve the winding number and edge (boundary) states' low energy physics for the number of edge states invariant, and this is where the relationship gets its name.

Consider the fully dimerized limit again, as shown in Figure 2.12. The edge states are not limited to the two boundaries of the chain. By dividing the bulk into different domains, we can have edge states between different insulating domains at the domain walls. One edge state in the bulk domain is a single isolated site; because the onsite potential is not allowed, the site is a zero energy state. Another example is a trimer where the two edges form a zero energy eigenstate considering the odd superposition, that is:

$$H(|N, B\rangle - |N+1, B\rangle) = 0 \tag{2.28}$$

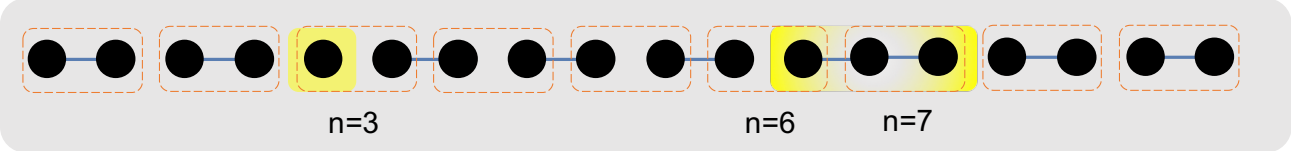

Figure 2.12: Fully dimerized SSH chain. The chain has three domains where the boundaries of the domains (domain walls) are represented by the yellow shading. The domain walls can be either localized like at the unit cell $n = 3$ or a superposition of two sites like the odd superposition at the trimer unit cells $n = 6$ and $n = 7$.

Now, consider a generic SSH chain with a domain wall (not the fully dimerized limit). Like the edge states at the generic SSH chain ends, the domain walls will have wavefunctions that decay exponentially into the bulk. Considering two separate domain walls, bonding and antibonding states will form at the walls' two edge states, that is, hybridize. In addition, the domain walls will hold half an electronic charge, a phenomenon called fractionalization.

2.9 Edge state solution

Consider an SSH model with N unit cells and where the intercell and intracell hopping amplitudes are $(1-\delta)$ and $(1+\delta)$, respectively. We can calculate the zero energy edge states as follows:

$$H = \sum_{m=1}^{N}((1+\delta_m)\left|m,B\right\rangle\left\langle m,A\right| + h.c.) + \sum_{m=1}^{N-1}((1-\delta_m)\left|m+1,A\right\rangle\left\langle m,B\right| + h.c.) \tag{2.29}$$

This Hamiltonian has a zero energy eigenstate if:

$$H\sum_{m=1}^{N}(a_m\left|m,A\right\rangle + b_m\left|m,B\right\rangle) = 0 \tag{2.30}$$

where we need to solve for a_m and b_m; hence, the above equation reduces to a 2N set of equations, as follows:

$$(1+\delta_m)a_m+(1-\delta_m)a_{m+1} = 0; \qquad (1-\delta_m)b_m+(1+\delta_m)b_{m+1} = 0; \qquad \text{where } m = 1,\ldots,N-1 \tag{2.31}$$

where the boundary equations are the following:

$$(1+\delta_N)a_N = 0; \qquad (1+\delta_1)b_1 = 0 \tag{2.32}$$

Solving for a_m and b_m using the first set of equations, we get:

$$m = 2, \ldots, N: \qquad a_m = \prod_{j=1}^{m-1} \frac{-(1+\delta_j)}{(1-\delta_j)} a_1 \tag{2.33}$$

$$m = 1, \ldots, N-1: \qquad b_m = \frac{-(1+\delta_N)}{(1-\delta_m)} \prod_{j=m+1}^{N-1} \frac{-(1+\delta_j)}{(1-\delta_j)} b_N \tag{2.34}$$

Obeying the boundary equations above results in:

$$b_1 = a_N = 0 \tag{2.35}$$

In the generic case of SSH, the above result establishes that there is no zero energy eigenstate $a_m = b_m = 0$. However, a zero energy state does not exist in the thermodynamic limit, $N \to \infty$; we can accept two approximate solutions by defining the bulk average values, where the average intercell hopping is stronger than the intracell. Hence, we define the following:

$$\overline{\log|(1+\delta)|} = \frac{1}{N-1}\sum_{m=1}^{N-1} \log|(1+\delta_m)|; \qquad \overline{\log|(1-\delta)|} = \frac{1}{N-1}\sum_{m=1}^{N-1} \log|(1-\delta_m)| \tag{2.36}$$

The solution for a_N and b_N becomes:

$$|a_N| = |a_1| e^{-(N-1)/\xi}; \qquad |b_1| = |b_N| e^{-(N-1)/\xi} \frac{|(1+\delta_N)|}{|(1+\delta_1)|} \tag{2.37}$$

where $\xi = \frac{1}{\overline{\log|(1-\delta)|} - \overline{\log|(1+\delta)|}}$ is the localization length. We can approximate the zero energy solutions using the bulk average values and $\xi > 0$, as follows:

$$|L\rangle = \sum_{m=1}^{N} a_m |m, A\rangle; \qquad |R\rangle = \sum_{m=1}^{N} b_m |m, B\rangle \tag{2.38}$$

Now, hybridizing the two states $|L\rangle$ and $|R\rangle$ under H will result in an exponentially small energy splitting. Using adiabatic elimination, we can estimate the splitting and energy eigenstates. Hence, the overlap is the following:

$$\langle R| H |L\rangle = \left|a_1 e^{-(N-1)/\xi}(1+\delta_N)b_N\right| e^{i\phi} \tag{2.39}$$

where $\phi \in [0, 2\pi)$. The approximation of the energy eigenstates are the following:

$$|0+\rangle = \frac{e^{-i\phi/2}|L\rangle + e^{i\phi/2}|R\rangle}{\sqrt{2}}; \qquad E_+ = \left|a_1 e^{-(N-1)/\xi}(1+\delta_N)b_N\right| \tag{2.40}$$

$$|0-\rangle = \frac{e^{-i\phi/2}|L\rangle - e^{i\phi/2}|R\rangle}{\sqrt{2}}; \qquad E_- = -\left|a_1 e^{-(N-1)/\xi}(1+\delta_N)b_N\right| \tag{2.41}$$

The above results show that the hybridized state's energy is exponentially small compared with the system size. The exact solution for uniform hopping can be written as in [25] as follows:

$$\left|\psi_{\pm}^{edge}\right\rangle = \sum_{n=0}^{M-1}(-)^n[\sinh\left((N-2n)\kappa\right)|2n+1\rangle \pm \sinh\left((2n+2)\kappa\right)|2n+2\rangle] \tag{2.42}$$

where N is even and $N = 2M$ and $k = \pi/2 + i\kappa$ and $\kappa = \frac{|log(r)|}{2} - \frac{r^N(1-r^2)}{2} + O(r^{2N})$ and $r = t_1/t_2$, which are the hopping parameters ratio. For an odd N, the solution is:

$$\left|\psi_0^{edge}\right\rangle = \sum_{n=0}^{M}(\frac{-t_1}{t_2})^n|2n+1\rangle \tag{2.43}$$

As we can see, there are two edge states for an even N, while there is only one edge state for an odd N, and their solutions are as given above.

2.10 Numerically computing the winding number

This section will discuss how to compute the winding number numerically. This method is adapted from [26]. The below method only works for closed systems. Let $j = N/2$ be the central unit cell and basis of states that we will work with, which is defined as follows:

$$|0_\eta\rangle = \sum_i \alpha_{\eta i} |\phi_i\rangle \tag{2.44}$$

where $(\eta = A, B)$ sites are localized on the cell, while $|\phi_i\rangle$ are the energy eigenstates of the Hamiltonian H. The energy eigenstates satisfy the following two conditions:

$$|\phi_{-i}\rangle = \Gamma |\phi_i\rangle$$

and $\quad \mathrm{E}_{-i} = -E_i \quad$ such that $\quad \cdots < E_{-2} < E_{-1} < 0 < E_1 < E_2 < \ldots$

where Γ is the chiral operator defined as $\Gamma = \Gamma_A - \Gamma_B$ ($\Gamma_{A,B}$ are the projectors onto the A or B sublattices, respectively). To solve it explicitly, let us define an operator M as follows:

$$M = \frac{Q_{BA}XQ_{AB} - Q_{BA}Q_{AB}X - Q_{AB}XQ_{BA} + Q_{AB}Q_{BA}X}{2} \tag{2.45}$$

where $Q = P_+ - P_-$ is the flat band analog to any generic Hamiltonian H, P_+ is the projector on the positive energy eigenstates, and P_- is the projector on the negative energy eigenstates. Then, we can rewrite Q as $Q = Q_{AB} + Q_{BA} = \Gamma_A Q \Gamma_B + \Gamma_B Q \Gamma_A$ (where Γ_A, Γ_B are projectors onto A and B sublattices respectively). Finally, X is the unit cell operator, which is a matrix with diagonal elements corresponding to the unit cell index. The winding number for the j unit cell is defined as:

$$v(j) = \sum_{\eta=A,B} \langle j_\eta | M | j_\eta \rangle \tag{2.46}$$

If we are only interested in the central unit cell $j = N/2$, the winding number becomes:

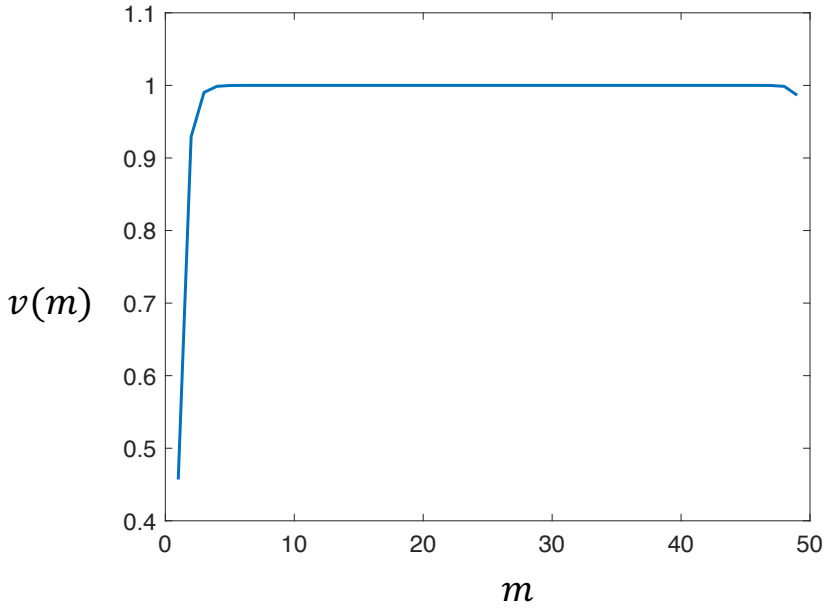

Figure 2.13: Winding number of the SSH model in the central region. We can see that the blue line has a winding number of 1. Here, $m = n/2$ is the index of the unit cell and n represents the lattice site along the chain of total length $N = 100$, where $\delta = 0.5$.

$$v(N/2) = \sum_{\eta=A,B} \langle (N/2)_\eta | \, M \, | (N/2)_\eta \rangle \tag{2.47}$$

where $|N/2\rangle$ has a negligible overlap with the edge states; we can use the identity $\Gamma_B Q = Q\Gamma_A$. Note that the chiral operator is local and diagonal in the position basis and that Γ_A and Γ_B are projectors, so the commutators $[X, \Gamma_A] = [X, \Gamma_B] = 0$. Hence, the winding number is:

$$v(N/2) = [\frac{((\Gamma_B Q \Gamma_A)(X_m \Gamma_A Q \Gamma_B - \Gamma_A Q \Gamma_B X_m) - (\Gamma_A Q \Gamma_B)(X_m \Gamma_B Q \Gamma_A - \Gamma_B Q \Gamma_A X_m))}{2}]_{[N/2,N/2]} \tag{2.48}$$

In Figure 2.13, we show the winding number along the SSH chain. We see that the local winding number is 1 in the middle of the chain for the topological phase $(\delta > 0)$ and N even.

2.11 End of Chapter

In 2016, Meier, An, and Gadway prepared the SSH model [27]. The SSH model is the basis for developing TI materials. These TI materials have many applications, such as enhancing photodetector [28,29], improving magnetic devices [30–32], working as more efficient field-effect transistors [33,34], and implementing topological quantum computation [16]. The previous applications resulted from extending the SSH model to 2D and 3D materials. The theoretical implication of the SSH model in photonic and phononic systems also revealed practical applications [35,36].

Chapter 3

Classical phononic model

The field of lattice vibration started with Einstein's Brownian motion theory and the discovery of atoms' existence in 1902 [37]. A decade later, Born and von Kàrmàn introduced the first lattice vibration model that laid down all the basic concepts for the modern theory of lattice vibration [38]. In this chapter, we discuss the diatomic chain, which is the typical starting point in most modern solid state physics books such as Kittel's book [39]; his book greatly influences this chapter. However, the existence of atoms was discovered in the 1900s; in [40], the authors claim that Lord Kelvin studied the behavior of diatomic lattices in the 1880s and presented them in his famous Baltimore lectures on molecular dynamics and wave theory of light in 1904 [41].

3.1 Diatomic chain

In current solid state physics books, two atoms per primitive cell model, which is also called the diatomic linear chain, is a model that studies a chain of atoms with alternating masses M_1 and M_2. This model is not an accurate representation of actual solids, but studying the model can give a good insight into the structure of such a system.

Before we start with the model, we need to clarify a fundamental approximation in the theory of lattice dynamics. For any neighboring atoms, the potential energy Φ between

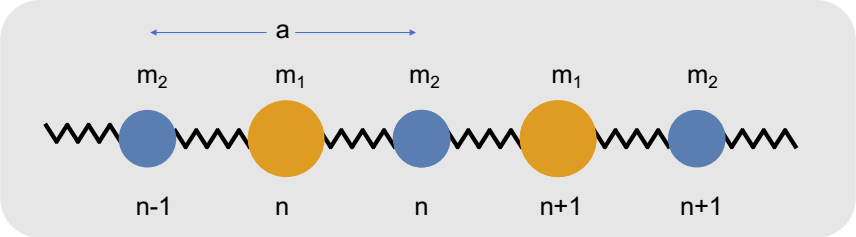

Figure 3.1: Diatomic chain with alternating masses m_1 and m_2 connected by springs.

the two atoms can be written as a Taylor expansion around the minimum point r_0, as follows:

$$\Phi(r) = \Phi_0 + \frac{1}{2}\frac{\partial^2\Phi}{\partial r^2}\Big|_{r_0} r_0(r - r_0)^2 + \frac{1}{3!}\frac{\partial^3\Phi}{\partial r^3}\Big|_{r_0} (r - r_0)^3 + \dots$$

The derivatives are executed at $r = r_0$, and in this case, the linear term is zero because, by definition, $\partial\Phi/\partial r$ is evaluated at the equilibrium distance r_0. This approximation is called the harmonic approximation, in which we neglect all terms with a power higher than two. However, the harmonic approximation might seem trivial and extreme, but its impact is powerful. The harmonic approximation is the only model with an exact solution in lattice vibration theory. Also, it can maintain many system features that persist after adding higher-order terms, such as the thermodynamic properties of materials, which we consider in chapter 5 when discussing thermal rectification.

Consider a chain of atoms M_1 and M_2 connected by springs with a force f, as seen in Figure 3.1. In this chapter, we take an infinite 1D chain, while in the next chapter, we consider a finite chain not fixed at the ends. We start with the equations of motion of this system; by Newton's law, we know that the coupling forces and forces of inertia are equal, so we have the following:

$$M_\alpha \ddot{u}_{n\alpha i} + \sum_{m\beta j} \Phi_{n\alpha i}^{m\beta j} u_{m\beta j} = 0 \tag{3.1}$$

where u is the displacement, α and β are the atoms in cell n, i and j are the spacial direction of the displacement, and $\Phi_{n\alpha i}^{m\beta j}$ is the coupling constant, which is the second derivatives of the potential, here defined as follows:

$$\frac{\partial^2 \Phi}{\partial r_{n\alpha i} \partial_{m\beta j}} = \Phi_{n\alpha i}^{m\beta j} \tag{3.2}$$

The chain in Figure 3.1 will only consider one directional component, i. While α and β equal 1 and 2, respectively, the m index has the values $n+1$,n, and $n-1$ because only the nearest neighbors interact. The equation of motion then becomes the following:

$$\begin{aligned} M_1 \ddot{u}_{n1} + \Phi_{n1}^{n-1,2} u_{n-1,2} + \Phi_{n1}^{n1} u_{n1} + \Phi_{n1}^{n2} u_{n2} = 0 \\ M_2 \ddot{u}_{n2} + \Phi_{n2}^{n1} u_{n1} + \Phi_{n2}^{n2} u_{n2} + \Phi_{n2}^{n+1,1} u_{n+1,1} = 0 \end{aligned} \tag{3.3}$$

We further assume the coupling constants $\Phi_{n1}^{n-1,2} = \Phi_{n1}^{n2} = \Phi_{n2}^{n1} = \Phi_{n2}^{n+1,1} = -f$ and $\Phi_{n1}^{n1} = \Phi_{n2}^{n2} = +2f$, so the equation of motion is:

$$\begin{aligned} M_1 \ddot{u}_{n1} + f(2u_{n1} - u_{n2} - u_{n-1,2}) = 0 \\ M_2 \ddot{u}_{n2} + f(2u_{n2} - u_{n1} - u_{n+1,1}) = 0 \end{aligned} \tag{3.4}$$

Because the lattice is periodic, we can use the below ansatz to find a solution, which can be done using a plane wave equation to represent the displacement $u_{n\alpha}$, as follows:

$$u_{n\alpha} = \frac{1}{\sqrt{M_\alpha}} u_\alpha(k) e^{i(nka - \omega t)} \tag{3.5}$$

By inserting the above plane wave ansatz into the equation of motions, we get the following:

$$
\begin{aligned}
(\frac{2f}{M_1} - \omega^2)u_1 - f\frac{1}{\sqrt{M_1 M_2}}(1 + e^{-ika})u_2 = 0 \\
-f\frac{1}{\sqrt{M_1 M_2}}(1 + e^{ika})u_1 + (\frac{2f}{M_2} - \omega^2)u_2 = 0
\end{aligned}
\tag{3.6}
$$

Thus, the dynamical matrix is the following:

$$
D(k) = \begin{bmatrix} \frac{2f}{M_1} & \frac{-f}{\sqrt{M_1 M_2}}(1 + e^{-ika}) \\ \frac{-f}{\sqrt{M_1 M_2}}(1 + e^{ika}) & \frac{2f}{M_2} \end{bmatrix}
\tag{3.7}
$$

This matrix is a straightforward eigenvalue/eigenvector equation, where ω^2 are the eigenvalues of the matrix, which has two solutions. Thus, this dynamical matrix has two normal modes. Because the matrix is Hermitian, the two eigenvalues should be real and can be either positive or negative. In cases where ω^2 is negative, it results in ω being imaginary. This case can be interpreted as the potential energy surface curved opposite to the displacements of atoms in the normal mode; that is, the crystal is unstable. From the above matrix, we can get the dispersion relation by subtracting the dispersion relation squared ω^2 from the above dynamical matrix and taking the determinant to be zero, such that:

$$
\det\{D(k) - \omega^2 \mathbb{1}\} = 0
\tag{3.8}
$$

$$
\omega^2 = f(\frac{1}{M_1} + \frac{1}{M_2}) \pm f[(\frac{1}{M_1} + \frac{1}{M_2})^2 - \frac{4}{M_1 M_2}\sin^2\frac{ka}{2}]^{1/2}
\tag{3.9}
$$

Thus, we can notice that the dispersion relation has a periodicity in k, which is one reciprocal lattice vector, that is:

$$
k = \frac{2\pi}{a}
\tag{3.10}
$$

The above periodicity does not only apply to one lattice; instead, we can show that this property can be generalized to all lattices, as follows:

$$D_{\alpha i}^{\beta j}(k) = D_{\alpha i}^{\beta j}(k+G) \qquad \text{where} \quad G \cdot r_n = 2\pi m \tag{3.11}$$

where $r_n = an$. Therefore, the above eigensolutions should meet the following conditions:

$$\omega(k) = \omega(k+G) \qquad \text{and} \quad \omega(-k) = \omega(k) \tag{3.12}$$

Examining the limiting cases at the Brillouin zone boundary can provide insights into what is happening inside the system. At the edge where k is very small, $k \approx 0$, we have the following:

$$\omega^2 = \omega_1^2 = 2f(\frac{1}{M_1} + \frac{1}{M_2}) - O(k^2) \qquad \text{and} \qquad \omega^2 = \omega_2^2 = \frac{f^2 a^2}{2(M_1+M_2)}k^2 \cong 0 \tag{3.13}$$

While in the limit where $k = \pi/a$, we have the following ω :

$$\omega^2 = \omega_1^2 = \frac{2f}{M_2} \qquad \text{and} \qquad \omega^2 = \omega_2^2 = \frac{2f}{M_1} \tag{3.14}$$

We call the branch ω_1 the optical branch and ω_2 the acoustic branch. The relationship between ω and k for $M_1 > M_2$ is shown in Figure 3.2. For $k = 0$ at the optical branch, the center of mass is fixed, while M_1 and M_2 move opposite each other. If M_1 and M_2 were two atoms of an opposite charge, this motion would be similar to a motion caused by an electromagnetic wave. The frequency of this kind of wave for some crystals is in the infrared frequency range. Thus, if the system describes a vibrating ionic crystal, the branch can be excited by an electric field of a light wave; hence, it is called an optical branch. While in the limit $k = 0$ at the acoustic branch, M_1, M_2, and their center of

mass movements are in the same direction. This motion is similar to a long wavelength acoustical vibration, which is where the name originated.

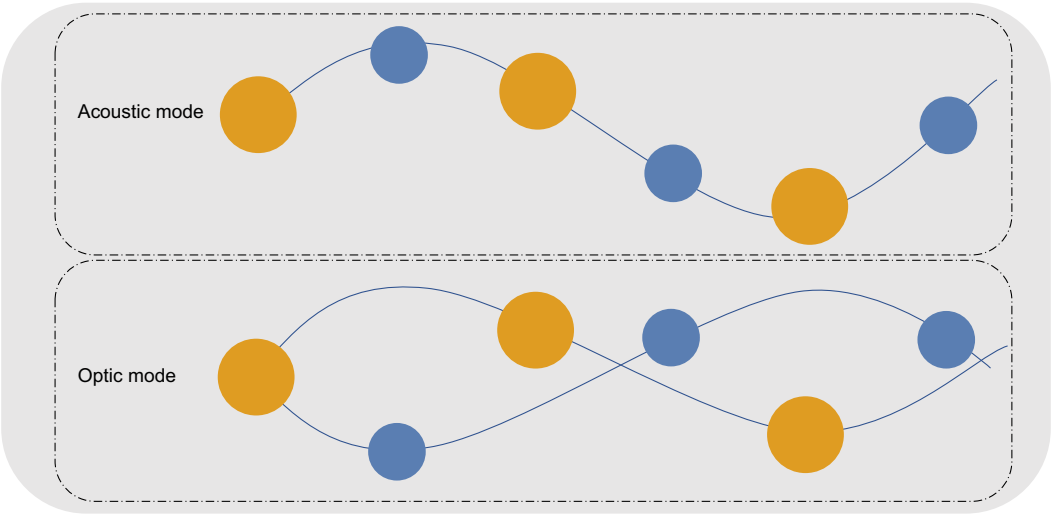

Figure 3.2: Two diagrams of the diatomic chain vibrations that show the acoustic mode vs. the optical mode.

At the $k = \pi/a$ limit, the solutions represent that one atom is stationary while the other is moving in the opposite direction to the moving atom in the neighboring unit cell. This limit makes it very hard to distinguish between optical and acoustic modes compared with the limit $k = 0$, where the distinction between in-phase/out–of–phase motions is obvious.

In Figure 3.3, we can see the full set of solutions for $\omega(k)$ for the values of k. The two curves represent optical and acoustic modes. Figure 3.3 shows multiple features of the model. At $k = \pi/a$, the system has zero group velocity, that is, $\partial\omega/\partial k = 0$ for both solutions. Thus, the waves are standing waves that correspond to atoms' motion being opposite to each other in each neighboring unit cell. Another feature is that the solutions for all k are invariant when changing the sign of k; that is, the solutions for k equal the solutions for $-k$. The last feature is that the solutions are invariant under the addition of a reciprocal lattice vector, which here is $\pm 2\pi n/a$.

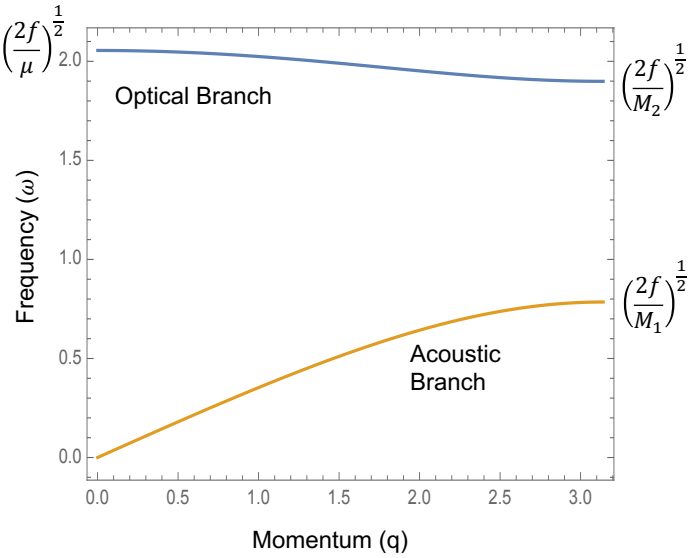

Figure 3.3: Dispersion relation of the diatomic chain with mass ratio $1/\mu = M_2/M_1 = 0.9$.

3.2 Phonons as quantization of elastic waves

In the previous section, we introduced a lattice vibration. When quantized, the energy of this vibration is called a phonon. In this section, we derive the phonon Hamiltonian into a set of harmonic oscillators. By using the same chain in the previous section, the displacement q of atom n can be expressed using the normal coordinate $Q_j(k)$, where k is the wavenumber, is as follows:

$$q_n^l = \frac{1}{\sqrt{Nm_n}}\left(\sum_{j,k\geq 0} a_{n,j}(k)e^{ikx_n^l}Q_j(k) + \sum_{j,k>0} a_{n,j}(-k)e^{-ikx_n^l}Q_j(-k)\right) \tag{3.15}$$

where:

$$Q_j(k) = \frac{1}{2}(A_{0,j}(k)e^{-i\omega_j(k)t} + A_{0,j}(k)e^{i\omega_j(-k)t}) = \frac{1}{2}(A_{0,j}(k)e^{-i\omega_j(k)t} + A_{0,j}^*(-k)e^{i\omega_j(k)t}) \tag{3.16}$$

So now the Hamiltonian is diagonalized as follows:

$$H = T + V = \frac{1}{2}\sum_{k,j}\{P_j(k)P_j^*(k) + Q_j(k)Q_j^*(k)\omega^2\} \tag{3.17}$$

where $Q^*(k) = Q(-k)$. Thus, the equation of motion from this Hamiltonian is:

$$\begin{aligned}\dot{Q}_j(k) &= \frac{\partial H}{\partial P_j^*(k)} = P_j(k) \\ \dot{P}_j(k) &= \frac{-\partial H}{\partial Q_j^*(k)}\end{aligned} \tag{3.18}$$

which gives:

$$\ddot{Q}_j(k) = \dot{P}_j(k) = -\omega_j^2 Q_j(k) \tag{3.19}$$

The above equation of motion is equivalent to an uncoupled 2N harmonic oscillator's motion.

Now, looking at the system quantum mechanically, $Q_j(k)$ and $P_j(k)$ should satisfy the following commutation relation, substituting $Q_j(k)$ and $P_j(k)$ with $\hat{Q}_j(k)$ and $\hat{P}_j(k)$, respectively:

$$\begin{aligned}[\hat{Q}_j^*(k), \hat{P}_{j'}(k')] = [\hat{Q}_j(k), \hat{P}_{j'}^*(k')] = i\hbar\Delta(k-k')\delta_{j,j'} \\ [\hat{Q}_j^*(k), \hat{Q}_j(k')] = [\hat{P}_j^*(k), \hat{P}_j(k')] = 0\end{aligned} \tag{3.20}$$

where $\Delta(k-k') = 1$ for $k = k' \pm 2\pi n/a$ and $\Delta(k-k') = 0$ otherwise.

Next, we define the creation operator $\hat{b}_j^\dagger(k)$ and annihilation operator $\hat{b}_j(k)$ as follows:

$$\begin{aligned}\hat{b}_j^\dagger(k) &= \sqrt{\frac{\omega_j(k)}{2\hbar}}\hat{Q}_j(k) - i\sqrt{\frac{1}{2\hbar\omega_j(k)}}\hat{P}_j(k) \\ \hat{b}_j(k) &= \sqrt{\frac{\omega_j(k)}{2\hbar}}\hat{Q}_j(k) + i\sqrt{\frac{1}{2\hbar\omega_j(k)}}\hat{P}_j(k)\end{aligned} \tag{3.21}$$

The Hamiltonian then becomes:

$$H = \frac{1}{2}\sum_{k,j}(\hat{P}_j^*(k)\hat{P}_j(k) + \omega_j^2\hat{Q}_j^*(k)\hat{Q}_j(k)) = \frac{1}{2}\sum_{k,j}\hbar\omega_j(\hat{b}_j^\dagger(k)\hat{b}_j(k) + \frac{1}{2}) \tag{3.22}$$

Thus, the system has a Hamiltonian similar to a 2N harmonic oscillator. Looking at the system as a harmonic oscillator makes it easy to adapt it so that it can incorporate quantum mechanics. However, starting with harmonic approximation does not explain some properties, such as thermal expansion and conductivity and behavior such as phase transitions. We can modify the model by introducing higher-order anharmonic terms, as needed. This technique has shown promising results, for example, by allowing the force constants to change to explain the thermal expansion.

3.3 End of chapter

Phonons' dispersion relation in 2D and 3D materials has been studied intensively [42, 43] because most production materials are in these two classes. However, 1D materials are less critical in commercial uses but have significant theoretical implications. The 1D diatomic chain dispersion relation has been validated experimentally recently [44, 45]. The theoretical implication of this simple 1D chain is practical in many fields, from efficient optical transmission [46] to acoustical devices [47]. Another essential concept regarding phonons is heat transport, which we will discuss in the last chapter.

Chapter 4

Topological phononic model

4.1 Phononic model setup

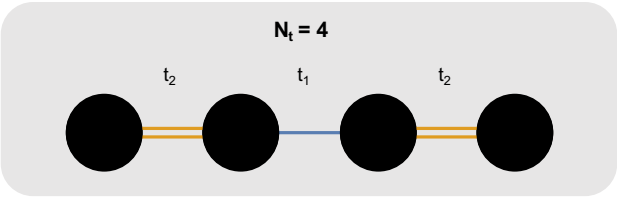

Figure 4.1: 1D chain of the SSH model.

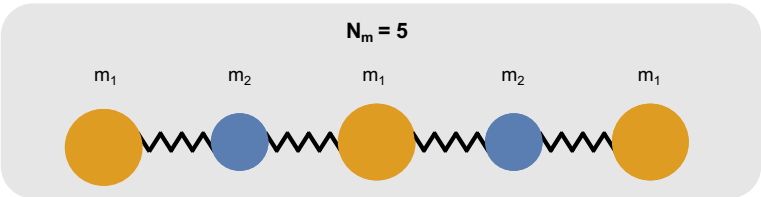

Figure 4.2: 1D chain of the phononic model.

We start with a diatomic chain of alternating masses (m_1 and m_2). These masses are connected by a spring with a spring constant k (as seen in Figure 4.2). We will show that these masses are analogous to the SSH model's intercell hopping parameters t_1 and t_2, while the spring constant corresponds to the sites in the SSH chain. The corresponding dynamical matrix is as follows:

$$H_m = \begin{bmatrix} \frac{k}{m_1} & -\frac{k}{m_1} & 0 & \dots & & \\ -\frac{k}{m_2} & \frac{2k}{m_2} & -\frac{k}{m_2} & 0 & \dots & \\ 0 & -\frac{k}{m_1} & \frac{2k}{m_1} & -\frac{k}{m_1} & 0 & \dots \\ \vdots & 0 & -\frac{k}{m_2} & \frac{2k}{m_2} & -\frac{k}{m_2} & 0 \\ & \vdots & 0 & \ddots & \ddots & \ddots \\ & & \vdots & 0 & -\frac{k}{m_n} & \frac{k}{m_n} \end{bmatrix} \qquad n = 2 \text{ (even) and } n = 1 \text{ (odd)} \qquad (4.1)$$

Below is a derivation for the phononical topology analogous to the SSH model, which can be found in Ref. [22]. Deriving the bulk momentum-space Hamiltonian, we can apply Bloch's theorem because the bulk is translation invariant. The Bloch eigenstates are as follows:

$$|\Psi_n(p)\rangle = |p\rangle \otimes |u_n(p)\rangle$$

where $|p\rangle = \frac{1}{\sqrt{N}} \sum_{m=1}^{N} e^{imp} |m\rangle$, for $p \in \{\delta_p, 2\delta_p, \dots, N\delta_p\}$ with $\delta_p = \frac{2\pi}{N}$ and $|u_n(p)\rangle = a_n(p) |A\rangle + b_n(p) |B\rangle$. We apply Fourier transform only on the external degree of freedom to have periodicity in the Brillouin zone.

$$\hat{H}(p + 2\pi) = \hat{H}(p); \qquad |u_n(p + 2\pi\rangle = |u_n(p)\rangle$$

4.2 Phononic model dispersion relation

Solving for the eigen energies and $\hat{H} |\Psi_n(p)\rangle = \omega^2 |\Psi_n(p)\rangle$, we get the following:

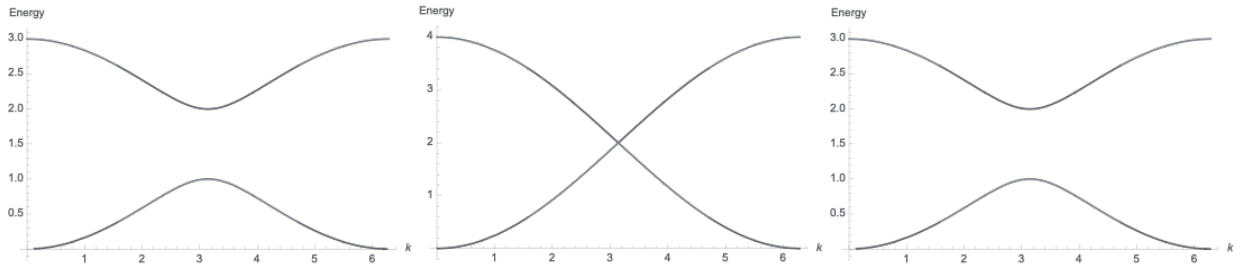

Figure 4.3: Dispersion relation of SSH and phononic of the infinite periodic lattice.

$$\begin{bmatrix} \frac{k}{m_1} & -\frac{k}{m_1} & 0 & \dots & & & \\ -\frac{k}{m_2} & \frac{2k}{m_2} & -\frac{k}{m_2} & 0 & \dots & & \\ 0 & -\frac{k}{m_1} & \frac{2k}{m_1} & -\frac{k}{m_1} & 0 & \dots & \\ \vdots & 0 & -\frac{k}{m_2} & \frac{2k}{m_2} & -\frac{k}{m_2} & 0 & \\ & \vdots & 0 & -\frac{k}{m_1} & \frac{2k}{m_1} & -\frac{k}{m_1} & 0 \\ & & \vdots & 0 & \ddots & \ddots & \\ & & & \vdots & 0 & -\frac{k}{m_n} & \frac{k}{m_n} \end{bmatrix} \begin{bmatrix} A \\ B \\ Ae^{ip} \\ Be^{ip} \\ \vdots \\ Ae^{iNp} \\ Be^{iNp} \end{bmatrix} = E(k) \begin{bmatrix} A \\ B \\ Ae^{ip} \\ Be^{ip} \\ \vdots \\ Ae^{iNp} \\ Be^{iNp} \end{bmatrix} \tag{4.2}$$

Thus, the matrix $H(p)$ of the bulk momentum-space hamiltonian is as follows:

$$H(p) = \begin{bmatrix} \frac{2}{m_1} & -\frac{1}{m_1}(1+e^{-ip}) \\ -\frac{1}{m_2}(1+e^{ip}) & \frac{2}{m_2} \end{bmatrix} \tag{4.3}$$

$$E(p) = \frac{\pm\sqrt{m_1^2+m_2^2+2m_1m_2\cos(p)}+m_1+m_2}{m_1m_2} \tag{4.4}$$

$$\Psi(p) = \left(\frac{\pm e^{-ip}\sqrt{e^{2ip}(m_1^2+m_2^2+2m_1m_2\cos(p)}+m_1+m_2}{m_1m_2}, 1 \right)' \tag{4.5}$$

Calculating the eigenvalues of the above matrix and plotting the result, we get the dispersion relations shown in Figure 4.3.

The above results are the infinite case where the phononic model dispersion relation matches the topological phase changes in 1D topological insulator dispersion relations.

For the finite case, we need to transform our matrix to show the equivalency, and we let $k = 1$.

$$\tilde{H} = m_1 m_2 H - (m_1 + m_2) I \tag{4.6}$$

$$\tilde{H} = \begin{bmatrix} -m_1 & -m_2 & 0 & \dots & & \\ -m_1 & m_1 - m_2 & -m_1 & 0 & \dots & \\ 0 & -m_2 & m_2 - m_1 & -m_2 & 0 & \dots \\ \vdots & 0 & -m_1 & m_1 - m_2 & -m_1 & 0 \\ & \vdots & 0 & \ddots & \ddots & \ddots \\ & & \vdots & 0 & -\overline{m}_n & -m_n \end{bmatrix} \qquad \overline{m}_n = \begin{cases} m_1 \text{ if } m_n = m_2, \\ m_2 \text{ if } m_n = m_1 \end{cases} \tag{4.7}$$

$$-\tilde{H} \begin{bmatrix} y_1 \\ y_2 \\ y_3 \\ y_4 \\ \vdots \\ y_{N-1} \\ y_N \end{bmatrix} = E \begin{bmatrix} y_1 \\ y_2 \\ y_3 \\ y_4 \\ \vdots \\ y_{N-1} \\ y_N \end{bmatrix}$$

Because the SSH model is one element less than the phononic model, the above Dynamical matrix can be reduced to the following:

$$\begin{bmatrix} 0 & m_1 & \dots & & & \\ m_1 & 0 & m_2 & 0 & \dots & \\ 0 & m_2 & 0 & m_1 & 0 & \dots \\ \vdots & 0 & m_1 & 0 & m_2 & 0 \\ & \vdots & 0 & \ddots & \ddots & \ddots \\ & & \vdots & 0 & m_1 & 0 \end{bmatrix} \begin{bmatrix} y_1 - y_2 \\ y_2 - y_3 \\ y_3 - y_4 \\ y_4 - y_5 \\ \vdots \\ y_{N-1} - y_N \end{bmatrix} = E \begin{bmatrix} y_1 - y_2 \\ y_2 - y_3 \\ y_3 - y_4 \\ y_4 - y_5 \\ \vdots \\ y_{N-1} - y_N \end{bmatrix} \tag{4.8}$$

As we can see, equation 4.7 has no chiral symmetry but equation 4.8 does, also the transformed matrix is similar to the SSH model, and the chiral symmetry is preserved in the phononic model because there are no diagonal elements in the matrix. Therefore, we can have an edge state analogous to the SSH. Comparing the transformed phononic Dynamical matrix to the SSH model is shown below.

The SSH and phononic models give identical bandgap and topological edge states in infinite and finite cases. The energies of the transformed mass-spring Hamiltonian have extra energy because of an additional mass in the phononic chain compared with the SSH chain. Figure 4.4 does not include the extra energy, though the value of that extra energy is $E = m_1 + m_2$. As we can see in Figure 4.4, the remaining energies are the same. One notable difference is that the positive energies are shifted by one in terms of k. Also, we look at $(y_{n-1} - y_n)$ instead of (y_n).

This means that if we consider the difference in displacement between neighboring masses, the corresponding dynamical matrix can be mapped exactly onto the SSH model. Note that the winding number calculated for $(y_n - y_{n-1})$ using the method in chapter two is equal to 1 for $m_1 < m_2$ and to 0 for $m_1 > m_2$. However, computing the winding number for y_n does not yield 1 or 0. The extra eigenvalue of equation 4.7 breaks the chiral symmetry. Therefore, $(y_n - y_{n-1})$ is topological, but (y_n) is not. Here the mass-spring system with size N is equivalent to the SSH model with size $N - 1$.

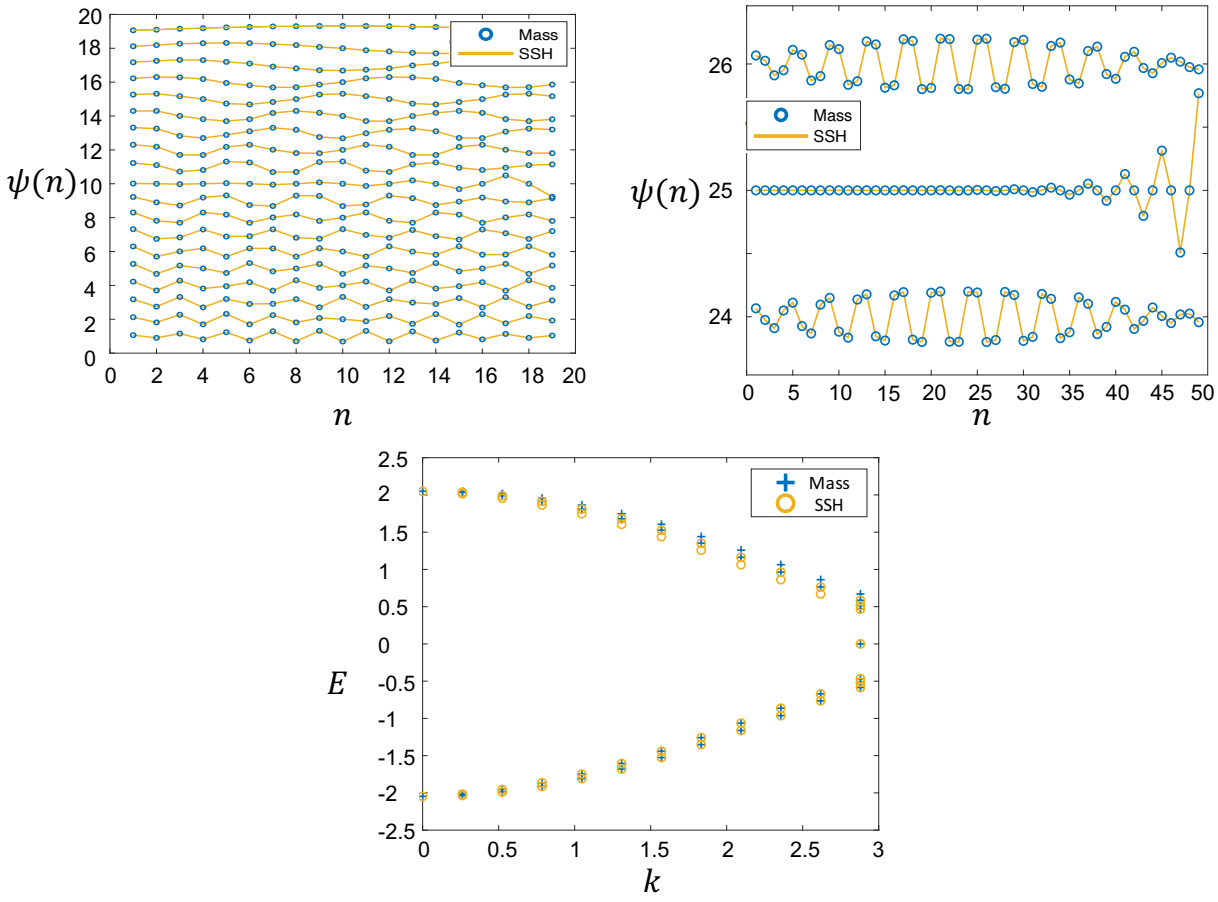

Figure 4.4: Top left: Numerical solution of the eigenvectors for the transformed phononic model of size 20 and SSH model of size 19, which shows all eigenvectors shifted by 1. Top right: Numerical solution of the eigen vectors for the transformed phononic model of size 50 and SSH model of size 49, which shows three eigenvectors (the central and the nearest two). Bottom: Numerical solution of eigen energies for the transformed phononic model and SSH model of size 50 and 49, respectively.

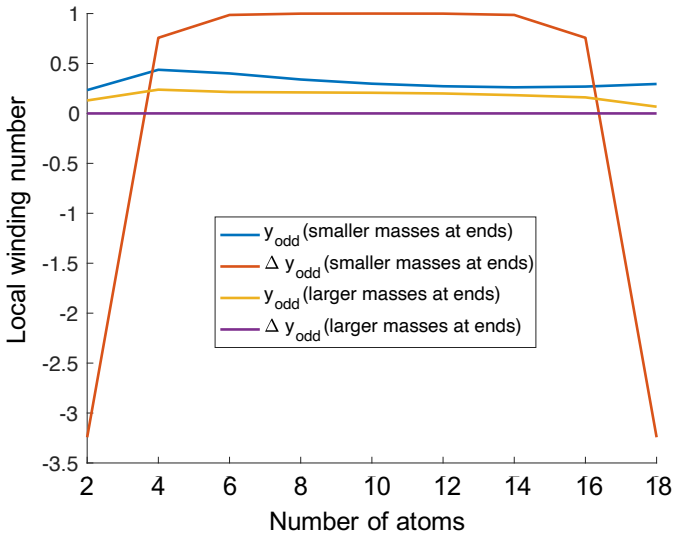

Figure 4.5: The local winding number of the original and transformed dynamical matrix for two cases starting with a smaller or larger mass. For chains of size n=19, the local winding number is one for the Δy case when we start with the smaller mass, while it is zero for the case when we start with the larger mass.

4.3 Phononic crystals

In this section, we design a 1D elastic phononic crystal (PC) that simulates our alternating mass model. PCs are manufactured materials constructed from a periodical structure of different geometries. PCs are attractive because they behave under specific conditions like tight-binding models, that is, they have a band gap. In 2015, the topology of a 1D phononic crystal acoustic system was investigated [48]. Then, a few other variations of phononic crystals with various geometries and materials were explored to understand the topology of these systems [49, 50].

The 1D crystal consists of a stainless steel beam with an alternating cross-sectional radii, as shown in Figure 4.6. The alternating cross-section allows us to see the topological properties of such a system. The below table shows the material's properties in a simulation of the system. The specifications are selected to obtain an experimentally convenient frequency with an inexpensive setup. The system can loosely be interpreted as the phonons are in the beam and the change of radius makes it a superlattice.

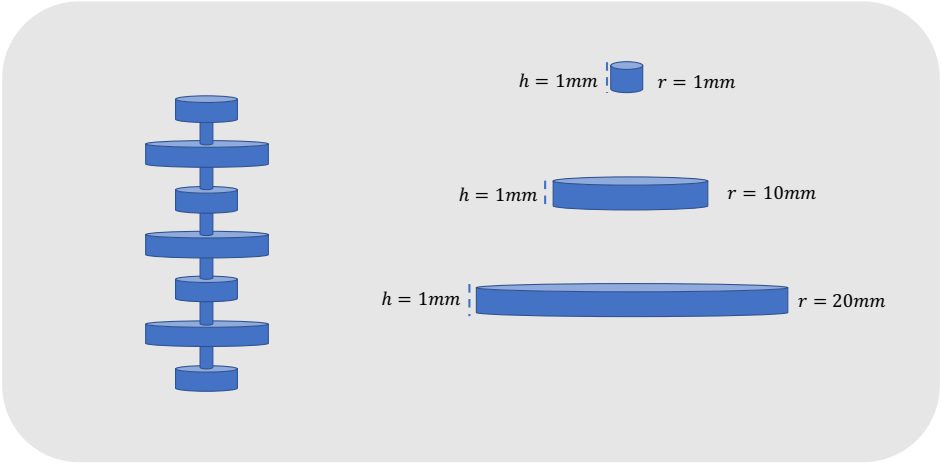

Figure 4.6: 1D phononic crystal beam geometry and details.

Material	Young's modulus (E)	Density (ρ)	Possion's ratio
Stainless steel	200 GPa	8060 kg/m^2	0.27

Table 4.1: Material specification of the PC.

4.3.1 Discretizing the 1D phononic crystal

After constructing the phononic crystal, we decided to discretize it to test the extreme limits and see how the system behaves. This geometry is easy to discretize because we have cylinders with different cross-sectional areas, so the only variable in this case is the radius r_i. Figure 4.7 represents a unit cell discretization. Then, the discretized mass and spring constant k are as follows:

$$m_i = \rho A_i \Delta x \qquad k_i = \frac{EA_i}{\Delta x} \tag{4.9}$$

where ρ is the material density, E is the Young's modulus of the material, and $A_i = \pi r_i^2$.

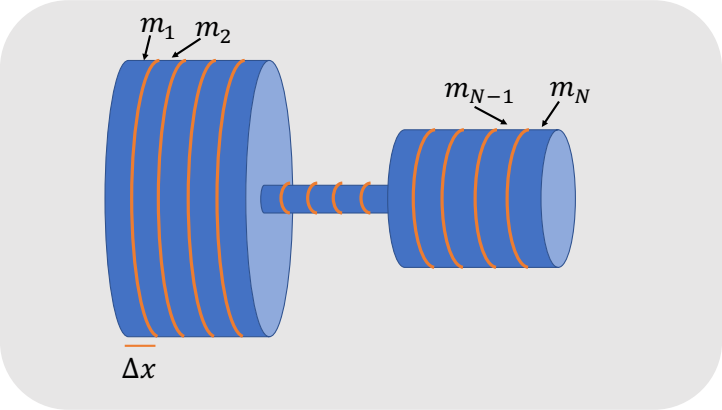

Figure 4.7: Discretizing the 1D phononic crystal.

We compare the phononic model of alternating masses with the discretized phononic crystal above (see also Figure 4.8). The dynamical matrix is as follows (assuming $\Delta x = L/i$, where L is the length of each element, assumed all equal):

$$DM = \begin{bmatrix} \frac{k_1}{m_1} & -\frac{k_1}{m_1} & 0 & \dots & \\ \frac{k_1}{m_2} & \frac{k_1+k_2}{m_2} & -\frac{k_2}{m_2} & 0 & \dots \\ 0 & -\frac{k_2}{m_3} & \frac{k_2+k_3}{m_3} & -\frac{k_3}{m_3} & 0 \\ \vdots & 0 & \ddots & \ddots & \ddots \\ & & 0 & -\frac{k_N}{m_N} & \frac{k_N}{m_N} \end{bmatrix}$$

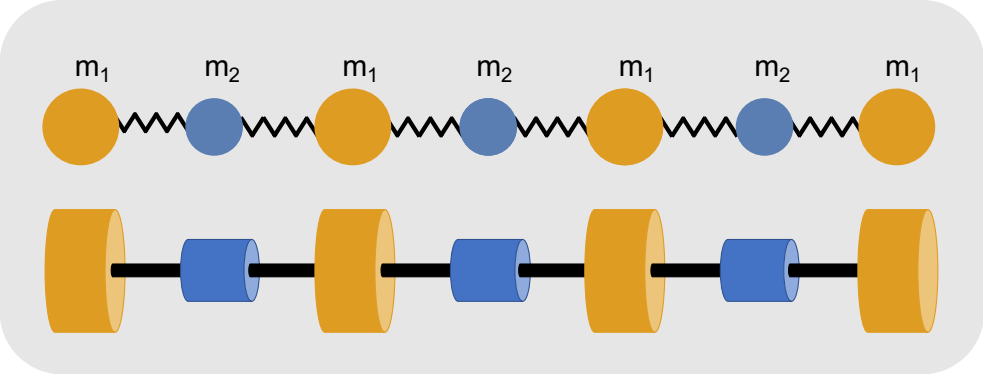

Figure 4.8: Comparing the phononic model of alternating masses (TB), shown on top and continuous phononic crystal, shown at the bottom.

Then, we ran the Matlab code to compute and plot the wavefunctions and frequencies of the two models to compare them. We used the $[V, D] = eig(DM)$ function, which returns two vectors V and D that represent the wavefunction and frequency, respectively. The results are shown in Figures 4.9 and 4.10.

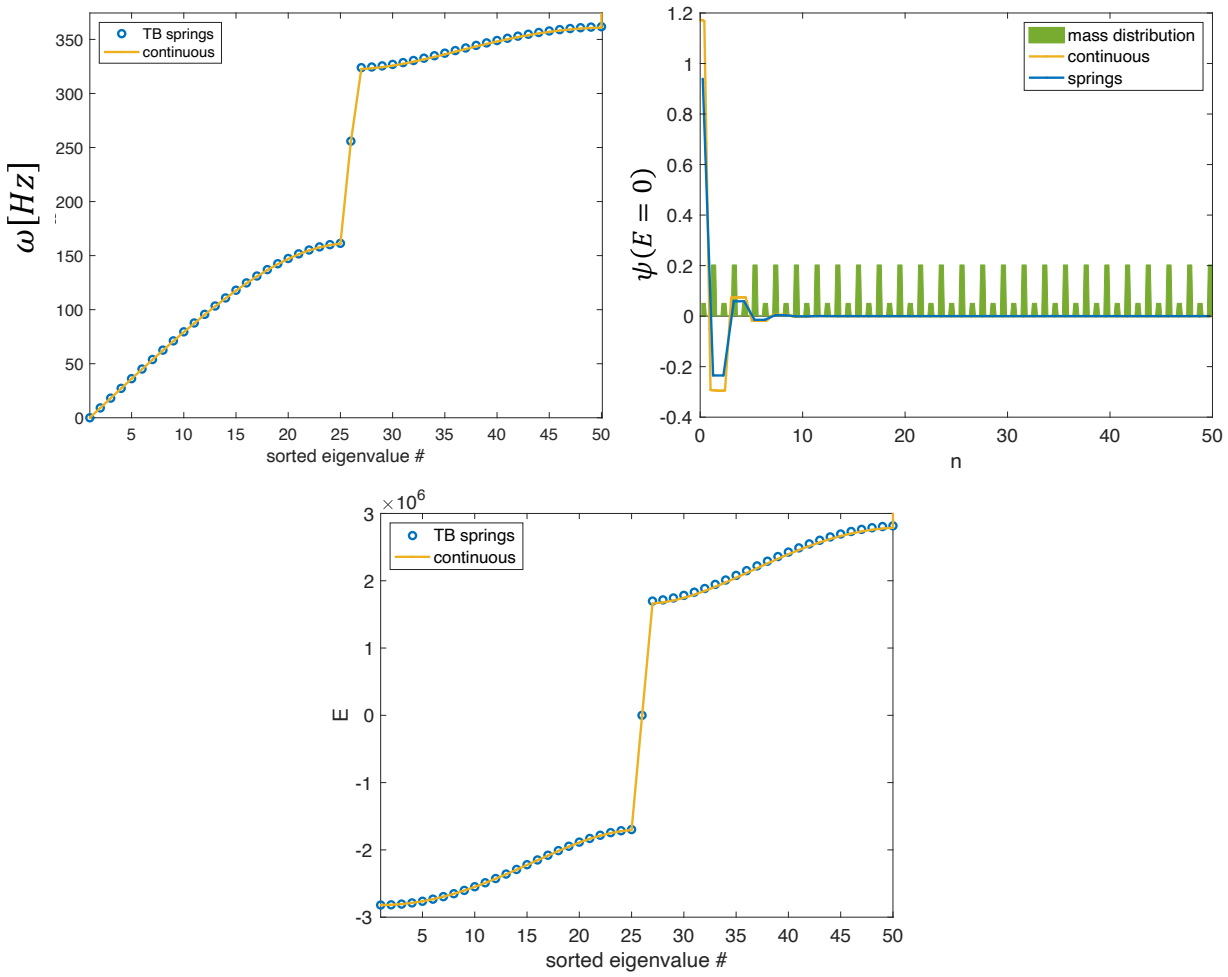

Figure 4.9: Starting with the smaller mass (even case). Top right: the wavefunction and Top left: the frequency of phononic model and descrtized PC systems of size 50. Bottom: The energy in terms of $E = \omega^2 - \frac{(m_1+m_2)k}{m_1 m_2}$. These results were obtained using the numbers in Figure 4.6 and Table 4.1, where $\Delta x = 0.1mm$.

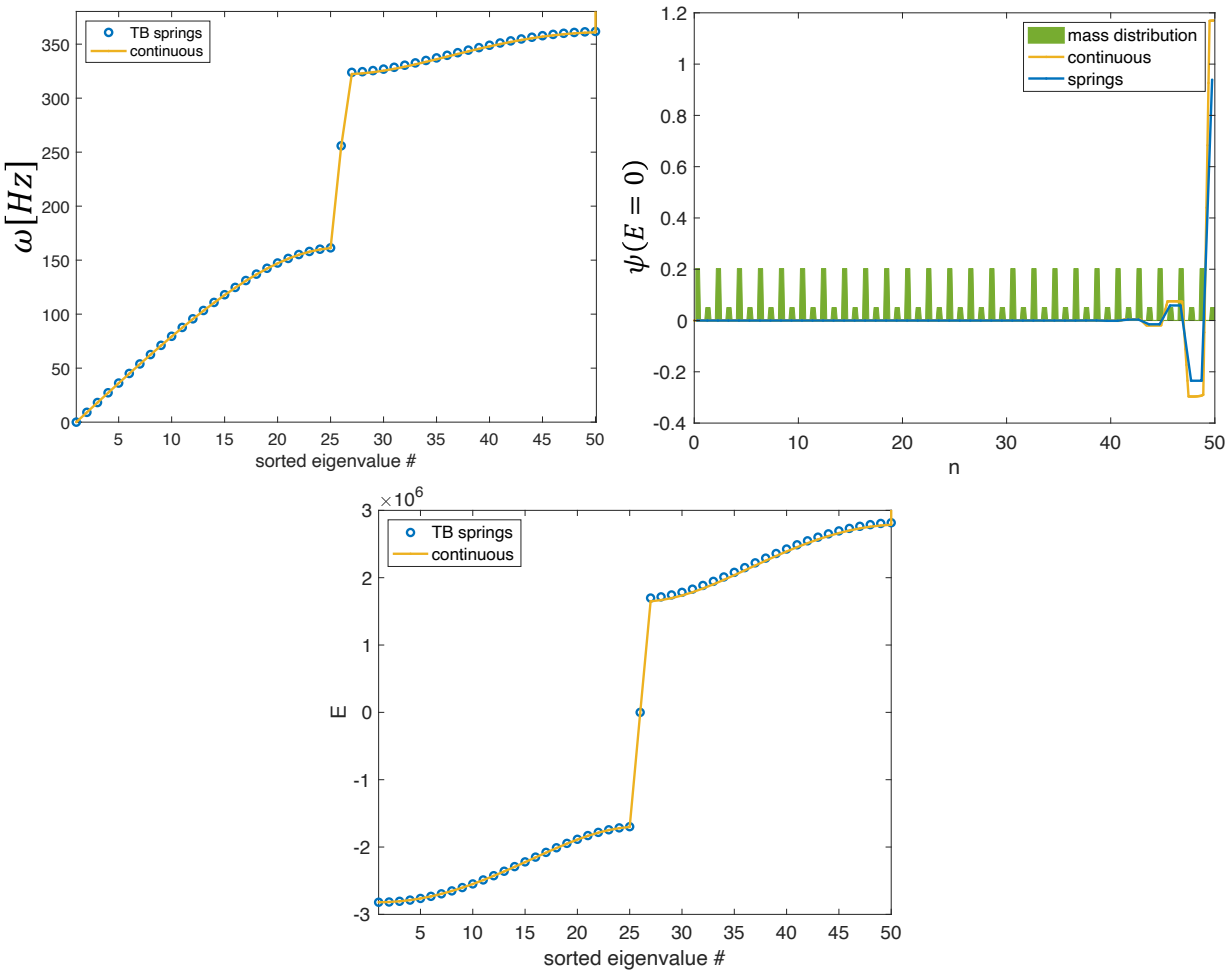

Figure 4.10: Starting with the larger mass (even case). Top right: the wavefunction and Top left: the frequency of phononic model and descrtized PC systems of size 50. Bottom: The energy in terms of $E = \omega^2 - \frac{(m_1+m_2)k}{m_1 m_2}$. These results were obtained using the numbers in Figure 4.6 and Table 4.1, where $\Delta x = 0.1mm$.

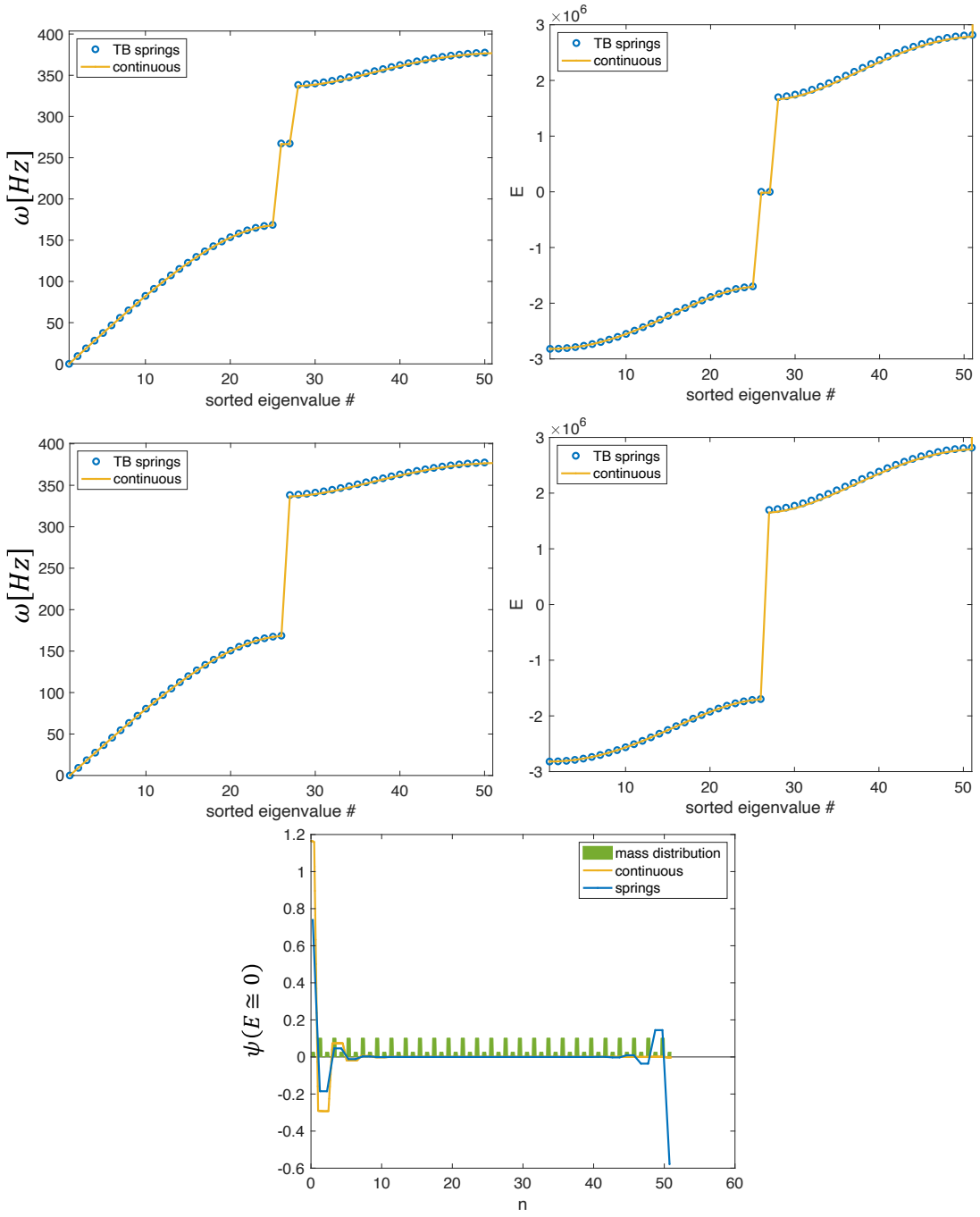

Figure 4.11: Top: Starting with the smaller mass (odd case). Top left: the frequency of phononic model and descrtized PC systems of size 51. Top right: The energy in terms of $E = \omega^2 - \frac{(m_1+m_2)k}{m_1 m_2}$. Middle: Starting with the larger mass (odd case). Middle left: the frequency of phononic model and descrtized PC systems of size 51. and Middle right: The energy in terms of $E = \omega^2 - \frac{(m_1+m_2)k}{m_1 m_2}$. Bottom: the wavefunction for the case that starts with the smaller mass (odd case). These results were obtained using the numbers in Figure 4.6 and Table 4.1, where $\Delta x = 0.1mm$.

4.4 End of Chapter

Figure 4.11 shows the topological and nontopological solutions for the odd masses case, which depends on the masses ratio m_1/m_2. When we start with the smaller mass, the system behaves topologically, whereas starting with the larger mass makes it non-topological. The above design of the experiment's results shown in Figures 4.9, 4.10, and 4.11 are experimentally realistic parameters. The next step would be to manufacture a beam of stainless steel with the specific requirements shown in Figure 4.6 and Table 4.1. The vibrations can be measured by vibration sensors. These vibration sensors could be a microphone (mechanical) or a vibrometer (optical). Then, the local winding number can be evaluated using the difference $(y_n - y_{n-1})$.

Chapter 5

Heat transport

Fourier introduced the law of heat conduction in the nineteenth century. As observed in various experiments, Fourier's law accurately describes heat transport phenomena; thus, it is considered a phenomenological law. The law states that the heat transfer rate through a material and temperature gradient are negatively proportional ($\vec{q} = -\kappa \nabla T$), where κ is the material conductivity constant. This equation gives rise to the heat diffusion equation when defining the local energy density $u(x,t)$, which satisfies the continuity equation $\frac{\partial u}{\partial t} + \nabla \cdot q = 0$.

$$\frac{\partial T(x,t)}{\partial t} = \frac{1}{c} \nabla \cdot [\kappa \nabla T(x,t)] \tag{5.1}$$

where c is the specific heat per unit volume $c = \partial u / \partial T$. The heat diffusion equation describes the heat carriers' motion: phonons, molecules, and electrons. These heat carriers move diffusively by going into random collisions. However, this picture of heat transport is valid for 3D materials; the description cannot be generalized to 1D and 2D materials. In recent years, theoretical physicists have been working on accurately describing 1D and 2D materials' heat transport phenomena [51]; Ref. [51] initiated this chapter. The two most common methods for studying heat transport in low dimensional systems are connecting the system to heat reservoirs, analyzing the nonequilibrium steady state, and studying the conductivity and equilibrium correlation function using the Green–Kubo relation.

5.1 Langevin baths

This section will focus on one method we have used in our research: the heat bath model, specifically Langevin baths. We also discuss the definition of temperature, heat current, and thermal conductivity in 1D systems. Here, consider a 1D chain of particles with the nearest neighbor interaction potential U. The 1D system is in an external potential V, and the Hamiltonian is as follows:

$$H = \sum_{l=1}^{N} [\frac{p_l^2}{2m_l} + V(x_l)] + \sum_{l=1}^{N-1} \frac{K}{2}(x_l - x_{l+1}) \tag{5.2}$$

where l denotes the particle's number, m_l is the particle's mass, x_l is the particle's position, and p_l is the particle's momentum. For simplicity we assume that the particles cannot cross each other and the interparticle potential ordering is maintained. In this case, a heat current will be induced by connecting the above Hamiltonian to heat reservoirs.

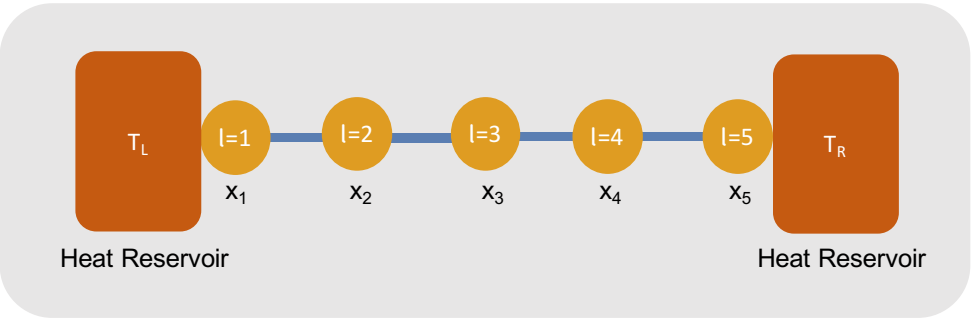

Figure 5.1: 1D Langevin model.

In the Langevin bath method, we represent heat reservoirs as additional force terms added to the edge particles (the particles in contact with the reservoirs, $l = 1$ and $l = N$). This additional force term is dissipative and behaves stochastically, forming Gaussian white noise. Thus, the equation of motion becomes the following:

$$
\begin{aligned}
\dot{p}_1 &= f_1 - \frac{\lambda}{m_1} p_1 + \eta_L(t) \\
\dot{p}_l &= f_l \quad \text{for} \quad l = 2, 3, \ldots, N-1 \\
\dot{p}_N &= f_N - \frac{\lambda}{m_N} p_N + \eta_R(t) \\
f_l &= -\frac{\partial H}{\partial x_l}
\end{aligned}
\tag{5.3}
$$

where f_l is the Newtonian force and $\eta_{L,R}$ are the stochastic terms corresponding to the left or right side, which is Gaussian, and λ is the dissipative term of the left or right side that fluctuates dissipatedly, as follows:

$$
\begin{aligned}
\langle \eta_L(t) \eta_L(t') \rangle &= 2\lambda T_L \delta(t - t') \\
\langle \eta_R(t) \eta_R(t') \rangle &= 2\lambda T_R \delta(t - t') \\
\langle \eta_L(t) \eta_R(t') \rangle &= 0,
\end{aligned}
\tag{5.4}
$$

where $T_{L,R}$ are the left and right reservoirs' temperatures and $\langle \cdot \rangle$ is the average over time.

5.2 Numerical computation of heat transport

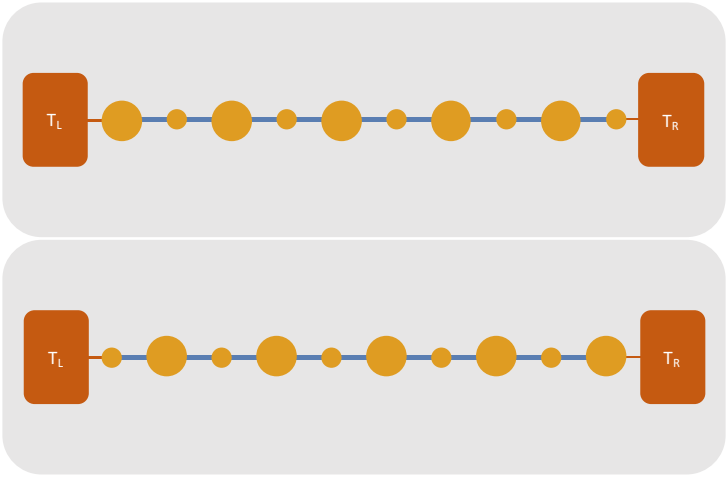

Figure 5.2: Langevin bath systems of size 10 (even case) with different arrangements of large and small masses. The orange line connecting the heat reservoirs to the masses is the coupling constant λ.

After defining the Langevin bath equations in the previous section, we implemented the equations using Matlab to investigate the heat transport of the system. We started with equation (5.3), where we defined $dt = 0.05$, all constants $k = 1$, and $0.5 \leq m_n \leq 2$. Our numerical accuracy is within the range of $dt\sqrt{k/m} \ll 1$ because the characteristic frequency is $\sqrt{k/m}$. Because our system consists of free–standing alternating masses, we picked a weak coupling constant λ connecting the right and left masses to the heat reservoirs, as in Figure 5.2. Then, we computed the Fourier transform of the displacement as a function of energy ($E = \omega^2$), where ω is the radial frequency (see Figure 5.3). The left figure in 5.3 shows different coupling constants' effects on the energy. In this case, the chain has an edge state at $E = m_1 + m_2 = 2.5$, where $m_1 = 0.5$ and $m_2 = 2$.

Furthermore, there are $N-1 = 20$ resonance energy levels in the band. Thermalization between the reservoirs and masses depends on the coupling, and for small coupling, the thermalization becomes slower. For the system to reach thermalization, the simulation must run long enough, as shown in Figure 5.3. For the time plot, we fixed the coupling constant $\lambda = 0.01$, and we computed the temperature of three masses m at $n = 1, 11, 21$.

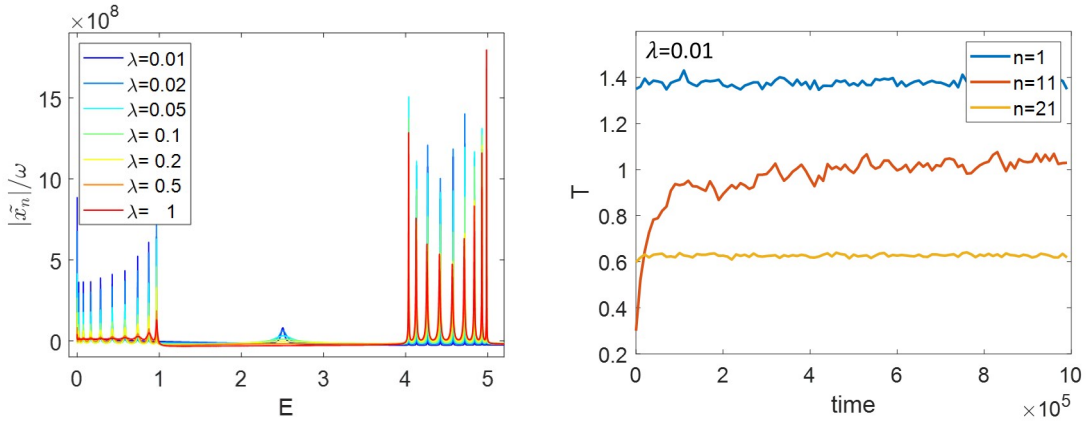

Figure 5.3: Left figure: Energy dependence of the Fourier transform of the mass displacement. The average of the absolute value for all the masses is shown for different values of the coupling to the thermal reservoirs λ. Right figure: The time dependence of the temperature for the first, middle, and last masses. A chain of length 21 is used here with $m_{2n+1} = 0.5$ and $m_{2n} = 2$ for n=1 to 10. Each time data point is averaged over $200,000$ time steps and 100 different configurations. Here, we used $T_L = 1.5$ and $T_R = 0.5$.

The time plot shows that the middle mass at $n = 11$ has the slowest thermalization rate, which saturates at time $t \sim 10^6$.

Now, we look at the temperature of each mass of the system. Using the fluctuation-dissipation theorem, we can solve for the temperature at each given mass in the chain. Because Boltzmann's constant of $k_B = 1$ is used in our choice of units, the fluctuation-dissipation theorem gives:

$$T_n = m_n \langle v_n^2 \rangle \tag{5.5}$$

The temperature dependence on sites are shown in Figure 5.4. The system we investigate is a chain of size $N = 21$ (the odd case). The two arrangements are either $m_1 < m_2$ and $m_1 > m_2$, and each configuration has a unique solution. For $m_1 < m_2$, the system exhibits a topologically nontrivial state with two edge modes. However, for $m_1 > m_2$, the system is topologically trivial with zero edge mode. For the topologically non-trivial case ($m_1 < m_2$), we see a strong temperature dependence near the edges, indicating the

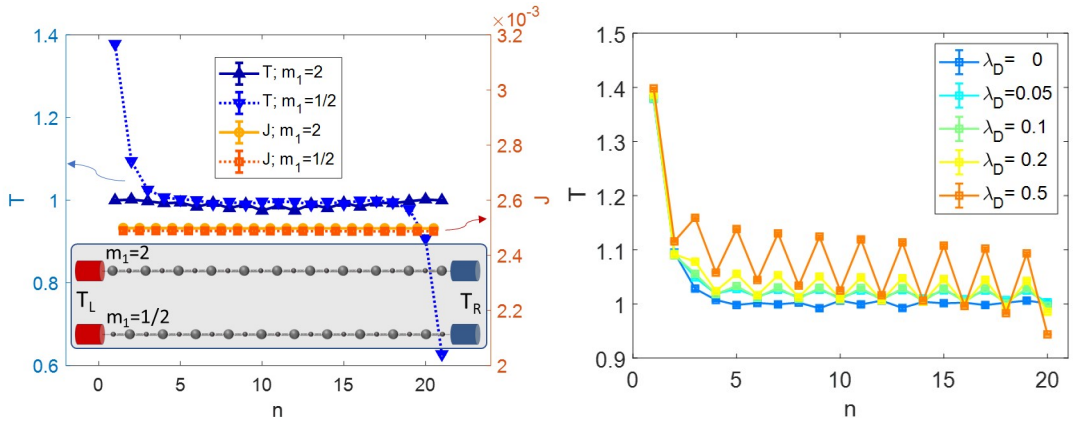

Figure 5.4: Left figure: Temperature dependence along the odd number chain ($N = 21$) shown on the left scale. The corresponding heat current is shown on the right scale. The two possible configurations of the odd number chains are shown in the illustration. Right figure: Temperature dependence along the even number chain ($N = 20$) for different values of the nonlinearity parameter λ_D. Here, $m_1 = 0.5$ and $m_2 = 2$. In both figures, the temperature of the left reservoir is 1.5 and 0.5 for the right reservoir; At time $t = 10^6$.

existence of edge states. However, in the other case, where there are no edge states, the system has no temperature variation. Thus, this case has no temperature dependence on the positions of the masses. To find the heat current of each of two consecutive masses (n and $n + 1$), we use the following equation:

$$J_{n+1/2} = -\frac{k}{2}\langle (v_n + v_{n+1})(x_{n+1} - x_n)\rangle \tag{5.6}$$

The above equation implies that the heat current does not depend on the position of the masses along the chain. Likewise, the heat current is independent of the presence or absence of the two edge states in the system. However, for the standard SSH model, the absence of the edge states results in electric current suppression at the band center. For clarification, we evaluate the classical heat transport, not the quantum heat transport. We would need to use a different phonon distribution for quantum heat transport, while here, we have used the classical Poisson temperature distribution because we are working with Langevin reservoirs.

5.3 Thermal rectification

Thermal rectification is a phenomenon in which thermal transport along a specific direction depends on the temperature gradient or heat current sign [52]. Thermal rectification is an exciting property, and an impressive outcome occurs if the alternating masses phononic system can exhibit this phenomenon. The even mass chain is a suitable candidate for thermal rectification because it has edge states at the chain edges, here depending on the mass ratio m_1/m_2. Thermal rectification develops when there is an asymmetric heat current exchange between the left and right reservoir and system. An essential element for thermal rectification is to have a nonlinear potential. Therefore, we introduce an additional non-linear potential in the Hamiltonian (5.2) with the following form:

$$V(x_n) = \lambda_D x_n^4 \tag{5.7}$$

where λ_D is the strength of the nonlinearity. Figure 5.4 shows the computed temperature per mass of an even chain with an asymmetric edge state configuration. The zero nonlinearity case has a comparable pattern to the odd chain of masses case, where there is a nonuniform temperature on the side at the edge state location. In the even chain presented in Figure 5.4, we set the smaller masses to be at the odd sites of the chain, which lead to an edge state at the left side of the chain. When we raise the nonlinearity, an exciting effect happens: the temperature along the chain oscillates with the higher temperature at the smaller masses. This is a result of the enhanced scattering from the nonlinear potential, which leads to an absolute heat current reduction, as shown in Figure 5.5.

To understand the heat rectification, we inverted the temperatures of the heat baths. Figure 5.5 shows a relative rise in rectification with the increasing nonlinearity. Notice that the absolute value of the heat current is larger for the case where the edge state and lower temperature bath are on the same side. By switching m_1 and m_2, the larger absolute heat current is inverted, thus creating a directional heat switch. However, the relative

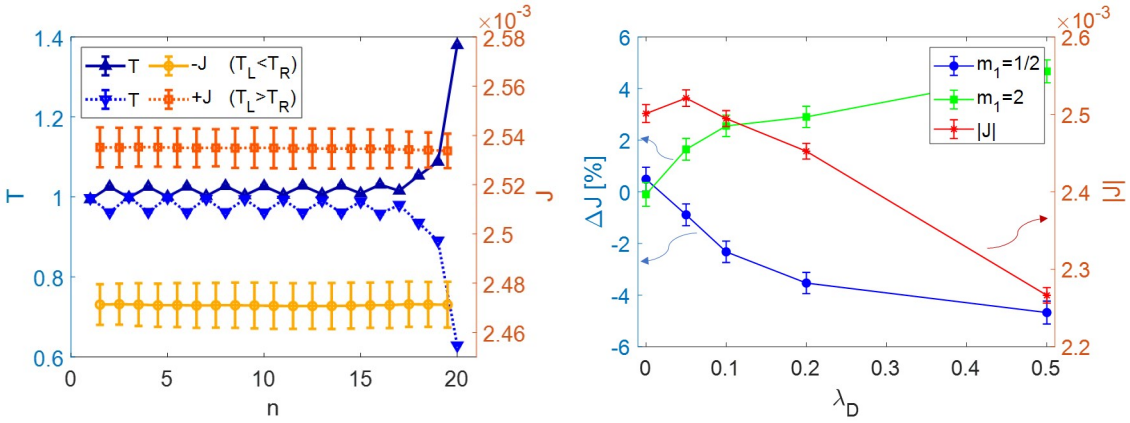

Figure 5.5: Left figure: Temperature dependence along the even number chain ($N = 20$) for a nonlinearity parameter $\lambda_D = 0.1$ and with $m_1 = 2$ and $m_2 = 0.5$. The absolute values of the heat currents are also shown for the two cases. Right figure: Dependence of the relative heat rectification on λ_D for the two cases ($m_1 = 0.5$ and $m_1 = 2$). The relative heat rectification is given by $\Delta J = 2\frac{J(T_L>T_R)+J(T_L<T_R)}{J(T_L>T_R)-J(T_L<T_R)}$. The absolute value of the heat current is depicted as a function of λ_D on the right scale.

rectification's relatively small, only a few percent, yet it is large enough to be observable in an experimental setup.

5.4 End of Chapter

Previous work has shown an alternating temperature distribution along the chain [19]; however, no rectification has been demonstrated. To conclude, the edge state structure of an alternating masses system SSH–like model can generate classical heat current rectification in the presence of nonlinear potential. The system's topological nature permits understanding heat rectification in 1D phononic materials that can be extended to higher dimensions using an alternating binary mass distribution, which is in contrast to a mass gradient along the chain. A topological graphene setup such as the Möbius graphene strip is a potential candidate for thermal rectification [53].

Chapter 6

Conclusion

Throughout the current thesis, we have studied the 1D chain of alternating atoms and their topological properties. Chapter one briefly introduced the significant milestones of the literature review that led to our present research thesis. These milestones in science started with topology, and then, the topological insulator was the first topology integration into physics. The success of the topological insulator led physicists to look for different systems that exhibit topological properties, such as topological phononics. Because heat transport is conducted through phonons, we briefly examined the concept of topological heat transport.

In chapter two, we learned the fundamental concepts of topology in condensed matter physics by exploring the SSH model. This chapter has provided the essential context for the work presented later in chapters four and five. We started with the tight binding model representation of metals, and then, we explored the band insulators to investigate the dispersion relations of conductors and insulators. After this, we introduced the SSH model, examined its topological properties, and defined the fundamental concepts of topology in condensed matter physics.

Chapter three formed a basis for the classical view of phonons, specifically the diatomic chain. We defined the dynamical matrix for the system and analyzed the dispersion relation of such a system.

Chapter four aimed to identify the topological behavior of our phononic model. Based on a comparative analysis of the SSH model and our phononic model, it can be concluded that phononic models with specific conditions can behave topologically. We further show the equivalence between the phononic and SSH models. By the end of chapter four, we proposed an experiment that can be conducted in future work to test the topological nature of the phononic crystal.

In chapter five, we analyzed heat transport for a topological phononic crystal. The results demonstrate that phononic crystals are practical when used as heat rectifiers. Our work opens the door to studying heat rectification in topological phononic crystals of different arrangements and dimensions.

Bibliography

[1] Leonhard Euler. Solutio problematis ad geometriam situs pertinentis. *Commentarii academiae scientiarum Petropolitanae*, pages 128–140, 1741.

[2] Springer Verlag GmbH, European Mathematical Society. Encyclopedia of Mathematics. Website. URL: `https://encyclopediaofmath.org/index.php?title=Topology,_general`. Accessed on 2022-11-14.

[3] Marcel Franz and Laurens Molenkamp. *Topological insulators*. Elsevier, 2013.

[4] K v Klitzing, Gerhard Dorda, and Michael Pepper. New method for high-accuracy determination of the fine-structure constant based on quantized hall resistance. *Physical review letters*, 45(6):494, 1980.

[5] Yi Gao, Tao Zhou, Huaixiang Huang, and Ran Huang. Majorana zero modes in the hopping-modulated one-dimensional p-wave superconducting model. *Scientific reports*, 5(1):1–9, 2015.

[6] DF Liu, AJ Liang, EK Liu, QN Xu, YW Li, C Chen, D Pei, WJ Shi, SK Mo, P Dudin, et al. Magnetic weyl semimetal phase in a kagomé crystal. *Science*, 365(6459):1282–1285, 2019.

[7] Yi Zhang, Ke He, Cui-Zu Chang, Can-Li Song, Li-Li Wang, Xi Chen, Jin-Feng Jia, Zhong Fang, Xi Dai, Wen-Yu Shan, et al. Crossover of the three-dimensional topological insulator bi 2 se 3 to the two-dimensional limit. *Nature Physics*, 6(8):584–588, 2010.

[8] Roman Süsstrunk and Sebastian D Huber. Observation of phononic helical edge states in a mechanical topological insulator. *Science*, 349(6243):47–50, 2015.

[9] W_P Su, JR Schrieffer, and Ao J Heeger. Solitons in polyacetylene. *Physical review letters*, 42(25):1698, 1979.

[10] Yizhou Liu, Xiaobin Chen, and Yong Xu. Topological phononics: from fundamental models to real materials. *Advanced Functional Materials*, 30(8):1904784, 2020.

[11] Samuel John Palmer, Yordan Ignatov, Richard V Craster, and Mehul Makwana. Asymptotically exact photonic approximations of chiral symmetric topological tight-binding models. *New Journal of Physics*, 2021.

[12] Hiromasa Wakao, Tsuneya Yoshida, Tomonari Mizoguchi, and Yasuhiro Hatsugai. Topological modes protected by chiral and two-fold rotational symmetry in a spring-mass model with a lieb lattice structure. *Journal of the Physical Society of Japan*, 89(8):083702, 2020.

[13] Xifang Xu, Wei Zhang, Jiaojiao Wang, and Lifa Zhang. Topological chiral phonons in center-stacked bilayer triangle lattices. *Journal of Physics: Condensed Matter*, 30(22):225401, 2018.

[14] Jiangxu Li, Lei Wang, Jiaxi Liu, Ronghan Li, Zhenyu Zhang, and Xing-Qiu Chen. Topological phonons in graphene. *Physical Review B*, 101(8):081403, 2020.

[15] Yizhou Liu, Nianlong Zou, Sibo Zhao, Xiaobin Chen, Yong Xu, and Wenhui Duan. Ubiquitous topological states of phonons in solids: Silicon as a model material. *Nano Letters*, 2022.

[16] Sankar Das Sarma, Michael Freedman, and Chetan Nayak. Majorana zero modes and topological quantum computation. *npj Quantum Information*, 1(1):1–13, 2015.

[17] Nianbei Li, Jie Ren, Lei Wang, Gang Zhang, Peter Hänggi, and Baowen Li. Colloquium: Phononics: Manipulating heat flow with electronic analogs and beyond. *Reviews of Modern Physics*, 84(3):1045, 2012.

[18] Jiangxu Li, Jiaxi Liu, Stanley A Baronett, Mingfeng Liu, Lei Wang, Ronghan Li, Yun Chen, Dianzhong Li, Qiang Zhu, and Xing-Qiu Chen. Computation and data driven discovery of topological phononic materials. *Nature communications*, 12(1):1–12, 2021.

[19] Venkateshan Kannan, Abhishek Dhar, and JL Lebowitz. Nonequilibrium stationary state of a harmonic crystal with alternating masses. *Physical Review E*, 85(4):041118, 2012.

[20] Chih-Chun Chien, Said Kouachi, Kirill A Velizhanin, Yonatan Dubi, and Michael Zwolak. Thermal transport in dimerized harmonic lattices: Exact solution, crossover behavior, and extended reservoirs. *Physical Review E*, 95(1):012137, 2017.

[21] Chih-Chun Chien, Kirill A Velizhanin, Yonatan Dubi, B Robert Ilic, and Michael Zwolak. Topological quantization of energy transport in micromechanical and nanomechanical lattices. *Physical Review B*, 97(12):125425, 2018.

[22] János K Asbóth, László Oroszlány, and András Pályi. A short course on topological insulators. *Lecture notes in physics*, 919:166, 2016.

[23] Adolfo G. Grushin. Introduction to topological phases in condensed matter, Spring 2021.

[24] Navketan Batra and Goutam Sheet. Understanding basic concepts of topological insulators through su-schrieffer-heeger (ssh) model. *arXiv preprint arXiv:1906.08435*, 2019.

[25] Meri Zaimi, Christian Boudreault, Nouédyn Baspin, Nicolas Delnour, Hichem Eleuch, Richard MacKenzie, and Michael Hilke. Detecting topological edge states with the dynamics of a qubit. *Physics Letters A*, 388:127035, 2021.

[26] Eric J Meier, Fangzhao Alex An, Alexandre Dauphin, Maria Maffei, Pietro Massignan, Taylor L Hughes, and Bryce Gadway. Observation of the topological anderson insulator in disordered atomic wires. *Science*, 362(6417):929–933, 2018.

[27] Eric J Meier, Fangzhao Alex An, and Bryce Gadway. Observation of the topological soliton state in the su–schrieffer–heeger model. *Nature communications*, 7(1):1–6, 2016.

[28] Marco Furchi, Alexander Urich, Andreas Pospischil, Govinda Lilley, Karl Unterrainer, Hermann Detz, Pavel Klang, Aaron Maxwell Andrews, Werner Schrenk, Gottfried Strasser, et al. Microcavity-integrated graphene photodetector. *Nano letters*, 12(6):2773–2777, 2012.

[29] Jiandong Yao, Jianmei Shao, Yingxin Wang, Ziran Zhao, and Guowei Yang. Ultrabroadband and high response of the bi 2 te 3–si heterojunction and its application as a photodetector at room temperature in harsh working environments. *Nanoscale*, 7(29):12535–12541, 2015.

[30] Jianshi Tang, Li-Te Chang, Xufeng Kou, Koichi Murata, Eun Sang Choi, Murong Lang, Yabin Fan, Ying Jiang, Mohammad Montazeri, Wanjun Jiang, et al. Electrical detection of spin-polarized surface states conduction in (bi0. 53sb0. 47) 2te3 topological insulator. *Nano letters*, 14(9):5423–5429, 2014.

[31] Matthias Götte, Tomi Paananen, Günter Reiss, and Thomas Dahm. Tunneling magnetoresistance devices based on topological insulators: ferromagnet–insulator–topological-insulator junctions employing bi 2 se 3. *Physical Review Applied*, 2(5):054010, 2014.

[32] AR Mellnik, JS Lee, A Richardella, JL Grab, PJ Mintun, Mark H Fischer, Abolhassan Vaezi, Aurelien Manchon, E-A Kim, Nitin Samarth, et al. Spin-transfer torque generated by a topological insulator. *Nature*, 511(7510):449–451, 2014.

[33] Jiwon Chang, Leonard F Register, and Sanjay K Banerjee. Topological insulator bi2se3 thin films as an alternative channel material in metal-oxide-semiconductor field-effect transistors. *Journal of Applied Physics*, 112(12):124511, 2012.

[34] Sanjay K Banerjee, II Leonard Franklin Register, Allan MacDonald, Bhagawan R Sahu, Priyamvada Jadaun, and Jiwon Chang. Topological insulator-based field-effect transistor, January 14 2014. US Patent 8,629,427.

[35] Z Turker, S Tombuloglu, and C Yuce. Pt symmetric floquet topological phase in ssh model. *Physics Letters A*, 382(30):2013–2016, 2018.

[36] Xun-Wei Xu, Yan-Jun Zhao, Hui Wang, Ai-Xi Chen, and Yu-Xi Liu. Generalized su-schrieffer-heeger model in one dimensional optomechanical arrays. *Frontiers in Physics*, page 795, 2022.

[37] Albert Einstein. Über die von der molekularkinetischen theorie der wärme geforderte bewegung von in ruhenden flüssigkeiten suspendierten teilchen. *Annalen der physik*, 4, 1905.

[38] M Born and Th Von Karman. On fluctuations in spatial grids. *Physikalische Zeitschrift*, 13(297-309):18, 1912.

[39] Charles Kittel, Paul McEuen, and Paul McEuen. *Introduction to solid state physics*, volume 8. Wiley New York, 1996.

[40] AA Maradudin, Paul Mazur, EW Montroll, and GH Weiss. Remarks on the vibrations of diatomic lattices. *Reviews of Modern Physics*, 30(1):175, 1958.

[41] Lord William Thomson Kelvin. *Baltimore lectures on molecular dynamics and the wave theory of light*. CUP Archive, 1904.

[42] Jérôme Olivier Vasseur, PA Deymier, G Frantziskonis, G Hong, B Djafari-Rouhani, and L Dobrzynski. Experimental evidence for the existence of absolute acoustic band

gaps in two-dimensional periodic composite media. *Journal of Physics: Condensed Matter*, 10(27):6051, 1998.

[43] R Sainidou, N Stefanou, and A Modinos. Linear chain of weakly coupled defects in a three-dimensional phononic crystal: A model acoustic waveguide. *Physical Review B*, 74(17):172302, 2006.

[44] Jakob Søndergaard Jensen. Phononic band gaps and vibrations in one-and two-dimensional mass–spring structures. *Journal of sound and Vibration*, 266(5):1053–1078, 2003.

[45] Anne-Christine Hladky-Hennion and Michel de Billy. Experimental validation of band gaps and localization in a one-dimensional diatomic phononic crystal. *The Journal of the Acoustical Society of America*, 122(5):2594–2600, 2007.

[46] H Liu, T Li, QJ Wang, ZH Zhu, SM Wang, JQ Li, SN Zhu, YY Zhu, and X Zhang. Extraordinary optical transmission induced by excitation of a magnetic plasmon propagation mode in a diatomic chain of slit-hole resonators. *Physical Review B*, 79(2):024304, 2009.

[47] Jérémy Cabaret, Vincent Tournat, and Philippe Béquin. Amplitude-dependent phononic processes in a diatomic granular chain in the weakly nonlinear regime. *Physical Review E*, 86(4):041305, 2012.

[48] Meng Xiao, Guancong Ma, Zhiyu Yang, Ping Sheng, ZQ Zhang, and Che Ting Chan. Geometric phase and band inversion in periodic acoustic systems. *Nature Physics*, 11(3):240–244, 2015.

[49] Jianfei Yin, Massimo Ruzzene, Jihong Wen, Dianlong Yu, Li Cai, and Linfeng Yue. Band transition and topological interface modes in 1d elastic phononic crystals. *Scientific reports*, 8(1):1–10, 2018.

[50] Yan Meng, Xiaoxiao Wu, Ruo-Yang Zhang, Xin Li, Peng Hu, Lixin Ge, Yingzhou Huang, Hong Xiang, Dezhuan Han, Shuxia Wang, et al. Designing topological interface states in phononic crystals based on the full phase diagrams. *New Journal of Physics*, 20(7):073032, 2018.

[51] Abhishek Dhar. Heat transport in low-dimensional systems. *Advances in Physics*, 57(5):457–537, 2008.

[52] Nick A Roberts and DG Walker. A review of thermal rectification observations and models in solid materials. *International Journal of Thermal Sciences*, 50(5):648–662, 2011.

[53] J. W. Jiang, J. S. Wang, and B. Li. Topology-induced thermal rectification in carbon nanodevice. *Europhysics Letters*, 89(4):46005, mar 2010.